On the Rotation and Propagation of Simulated Supercell Thunderstorms

RICHARD ROTUNNO AND JOSEPH KLEMP

National Center for Atmospheric Research,[1] *Boulder, CO 80307*

(Manuscript received 14 June 1984, in final form 18 October 1984)

ABSTRACT

We examine the rotation and propagation of the supercell-like convection produced by our three-dimensional cloud model. The rotation in the supercell is studied in terms of the conservation of equivalent potential vorticity and V. Bjerknes' first circulation theorem; neither of these have been used previously in this connection, and we find that they significantly contribute to the current level of understanding in this area. Using these we amplify the findings of our previous work in which we found that the source of midlevel rotation is the horizontally oriented vorticity associated with the environmental shear, while the low-level rotation derives from the baroclinic generation of horizontally oriented vorticity along the low-level cold-air boundary. We further demonstrate that these same processes that amplify the low-level rotation also produce the distinctive cloud feature known as the "wall cloud."

We find that the thunderstorm propagates rightward primarily because of the favorable dynamic vertical pressure gradient that, owing to storm rotation, is always present on the right flank of the updraft. Simulations without precipitation physics demonstrate that this rightward propagation occurs even in the absence of a cold outflow and gust front near the surface.

1. Introduction

The supercell thunderstorm has been shown to be amenable to three-dimensional numerical simulation (Klemp and Wilhelmson, 1978a,b; Wilhelmson and Klemp, 1978; Schlesinger, 1978; Thorpe and Miller, 1978; Klemp *et al.,* 1981). The three-dimensional airflow obtained in these models broadly conforms to that found in observational studies (Browning, 1964, 1965, 1968; Fankhauser, 1971); both models and observations show that the right-moving supercell's updraft is fed by the moist, potentially unstable air from low levels on its right (facing in the direction of storm motion) flank while the main downdraft, located on its left flank, is fed by the dry, potentially cold air at middle levels. The latter originates on the storm's right flank, passes round its forward flank and over to its left flank, and then descends nearly moist adiabatically due to evaporative cooling of precipitation falling from the leftward sloping updraft. This airflow pattern contains two distinctive features which observers recognize as hallmarks of supercell thunderstorms and which the three-dimensional models simulate. First, a supercell thunderstorm possesses a significant degree of organized rotation about a vertical axis, and second, the supercell thunderstorm propagates to the right of the mean tropospheric winds for periods that are long compared with the residence time of an air parcel within the storm. In the present work we seek to extend the current understanding of these phenomena through analysis of a model supercell thunderstorm. To do this, we introduce two analytical tools not previously used in studies of thunderstorm rotation: the conservation of equivalent potential vorticity and V. Bjerknes' first circulation theorem; and we use the technique developed by Rotunno and Klemp (1982) to study the dynamics of supercell propagation.

Experience with three-dimensional cloud models indicates that supercell-like convection is obtained by the model (as in nature) when there is a propitious combination of wind shear and latent instability in the environment (e.g., Weisman and Klemp, 1982). We study here a single numerical integration that produces a supercell-like storm broadly representative of the genus. This integration is performed in an environment which is nonrotating and, furthermore, where the wind shear vector does not vary direction with height. As discussed in Klemp and Wilhelmson (1978b), an initially symmetric thermal disturbance will remain symmetric about the wind shear vector as it grows and subsequently splits into two mirror-image storms, one cyclonically rotating, moving to the right of the mean wind, the other anticyclonically rotating, moving to the left. It is more commonly observed in the severe-storm environment that the wind shear vector veers with height (e.g., Maddox, 1976). Klemp and Wilhelmson (1978b) and Rotunno and Klemp (1982) have discussed how and why the right member of the split pair is favored and the left

[1] The National Center for Atmospheric Research is sponsored by the National Science Foundation.

member suppressed in this circumstance (and so have offered an explanation for the more common occurrence of rightward-moving cyclonically rotating supercell thunderstorms). Yet it is our experience that the supercell produced by the model in the more common case, where the wind shear vector veers with height, is very similar in its important attributes to the rightward-moving member of the split pair obtained in the unidirectional shear case. Because of the relative simplicity of the environmental shear in the latter case and the similarity of the resulting storm, we chose the latter as the subject for detailed study.

We find that there are two distinct physical mechanisms that account for updraft rotation. Both involve the upward tilting of horizontally oriented vorticity into the vertical, but we will show that the rotation at middle levels derives from the upward tilting of the horizontally oriented vorticity associated with the environmental shear (Barnes, 1970; Schlesinger, 1975; Rotunno, 1981), while the low-level rotation is generated by an entirely different process. At low levels, a significant amount of rain-cooled air from the storm's left flank is drawn into the updraft along with the warm air from the right. Our thesis is that the intense rotation at low levels in a supercell derives from the baroclinic generation of horizontally oriented vorticity along that part of the cool-air boundary situated upstream of the low-level updraft, and the subsequent upward tilting of this vorticity works to produce cyclonic vertically oriented vorticity (Klemp and Rotunno, 1983). We attempt to put these ideas into perspective in Section 3, where we study the full three-dimensional features of the vector vorticity field in the simulated storm. We also describe a first try at computing the circulation around a three-dimensional fluid curve surrounding the area of most intense rotation (at the time it occurs), then following the curve backwards in time to determine its evolution and the extent to which the circulation is either created or preserved as the curve evolves.

One motivation for studying the supercell storm that evolves in unidirectional shear is that the storm moves unambiguously to the right of the shear vector (or environmental wind shear is unidirectional and westerly; the storm moves in the east–west direction at some average of the east–west wind speed, yet also moves southward at a significant speed). In Section 4, we continue in the general direction of some earlier work on thunderstorm movements (Schlesinger, 1980; Rotunno and Klemp, 1982) in which methods were developed to discriminate between "dynamic" and "buoyant" forcing of the updraft. We find that the rightward propagation of our supercell is due to the favorable vertical gradient of dynamic pressure that persists on the right side of the updraft. We establish that this occurs because low pressure on the right flank of the updraft at middle levels is dynamically induced by the storm rotation. We advance the hypothesis that this is the primary mechanism by which storms propagate transverse to the mean wind. Although cold outflow is an important feature of supercells, it plays a largely passive role in the mechanics of transverse propagation. An idealized simulation where precipitation is not allowed is discussed and supports our contention.

Finally, in Section 5, we pay some attention to an often neglected aspect of cloud models: clouds. It has long been observed that tornadoes most often occur near the region where thunderstorm inflow and outflow meet (Ward, 1961; Golden and Purcell, 1978; Lemon and Doswell, 1979), with certain concomitant cloud formations (Fujita, 1959; Moller, 1978; Fankhauser *et al.*, 1983). Of particular interest to tornado aficionados are the lowered cloud base in the vicinity of the updraft (the wall cloud) and its appendage (the tail cloud) which forebode tornado formation. As already described, the airflow in a supercell may be characterized roughly as consisting of two major branches: warm, moist air rising and cool, dry air sinking. Some of the cool air being drawn into the updraft at low levels is extremely important for the development of low-level rotation, and we show how this flow pattern can explain the above-described cloud features which attend the tornado.

Before entering into the analysis, we present in Section 2 an overview of the simulation along with a *resumé* of relevant findings of past work. Section 6 contains a summary and our reflections on the still-outstanding theoretical problems.

2. An idealized supercell

Experience has taught us that almost all of the important features of a supercell thunderstorm can be simulated given the appropriate combination of latent static instability and wind shear; directional shear and environmental rotation are not essential factors. Consequently, in the present study we consider the development of an initially symmetric disturbance in the unidirectional, potentially unstable shear flow represented in Fig. 1 with the Coriolis force being neglected. The thermodynamic sounding is the same as that used by Klemp *et al.* (1981; their Fig. 2) to simulate the thunderstorms which occurred near Del City, OK on 20 May 1977, while the environmental wind profile is chosen to have a similar magnitude of shear as observed on that day but no directional change with height. The wind profile reflects our choice of a frame of reference in which the storm will not move in the x-direction. Since the shear vector is westerly we identify the south as "right" and the north as "left" in the ensuing discussion.

We use the three-dimensional cloud model developed by Klemp and Wilhelmson (1978a) to follow

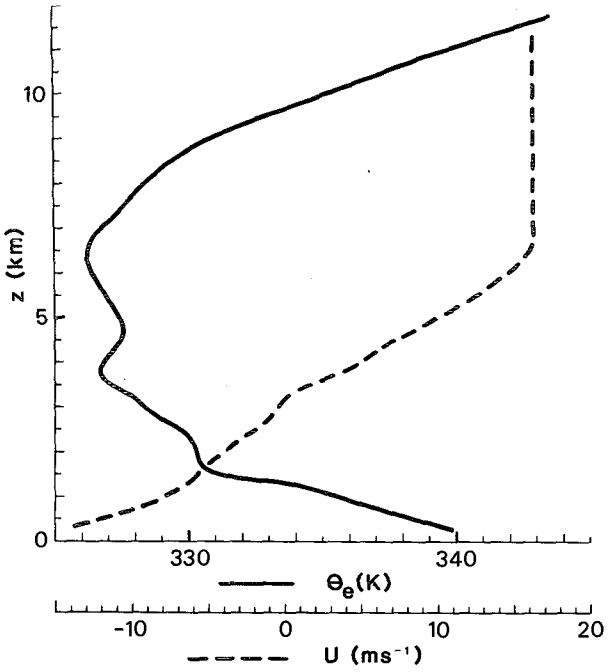

FIG. 1. Equivalent potential temperature θ_e (solid line) and the wind in the east–west direction U (dashed line) in the undisturbed environment.

the development of an initially symmetric perturbation through 160 min of real time. Because the disturbance develops with mirror-image symmetry about the shear vector, we compute the flow only for the right-moving member of the pair to conserve computer time. The simulation is carried out on a $54 \times 54 \times 16$ km domain with horizontal and vertical grid intervals set to 1 and 0.5 km respectively.

An overview of the evolution of the simulated storm is provided in Fig. 2 where the maximum vertical velocity is plotted as a function of time. The history of the maximum vertical velocity is similar to that described in Wilhelmson and Klemp (1978; hereafter WK), but because of the less unstable thermodynamic sounding and smaller domain used therein, the maximum updraft magnitude is about half that obtained herein. The initial increase of w_{max} reflects the growing initial cell, and the decrease at approximately $t = 20$ min indicates that the initial cell is going through its splitting stage. Thereafter, the maximum updraft undergoes a more or less steady increase as the split cell takes on the characteristics of a mature supercell thunderstorm. The basic description of cell splitting is provided by WK (see the discussion accompanying their Figs. 5–8). In order to emphasize several different aspects of the general development, we display here a similar series of plots: the flow fields at $t = 20$, 40 and 60 min at $z = 4$ and 0.25 km are shown in Figs. 3 and 4 respectively.

As the initial symmetric bubble of hot air rises, it remains warmer than its environment due to condensation and the release of latent heat, and so it accelerates upward (Fig. 3a). However, as the condensate accumulates and forms rain, the updraft becomes loaded and decelerates at its center (Figs. 3b, c). Also contributing to the negative buoyancy on the center axis is the evaporation of the condensate as it comes into contact with dry midlevel air. The latter enters the updraft on the center axis on the downshear side as a consequence of the vortex pair type of horizontal flow which occurs as an updraft forms in a unidirectional shear flow (Clark, 1979). Thus, one can identify at a very early stage the fundamental importance of the updraft rotation in bringing dry midlevel air into contact with rain and/or cloud so that the latter may evaporate and allow the air to descend nearly moist adiabatically. The result of this process is the formation of a pool of cold air on the left (northern) flank which is of crucial significance for the development of low-level rotation, as we will show in the next section. Although it is not immediately evident in Fig. 3, Schlesinger (1980) and Rotunno and Klemp (1982) showed that updraft growth is enhanced on the flanks of the initial cell through dynamical effects which also promote cell splitting. We return to this point in Section 4.

At $t = 60$ min, Fig. 3c shows a cyclonically rotating updraft with an anticyclonically rotating downdraft on the north flank, a commonly observed feature of supercell thunderstorms (Brandes, 1978; Klemp *et al.*, 1981). Here, as in the early stages, the rotating updraft brings air around from the forward or right to the left flank and into the downdraft. This point is substantiated in Section 5 where trajectory calculations are presented.

Figure 4a shows that at $t = 20$ min there is weak updraft in the region that contained the initial thermal perturbation. Figures 4b, c show the rain-cooled air, which originated at middle levels on the north flank and has now descended, spreading over the ground

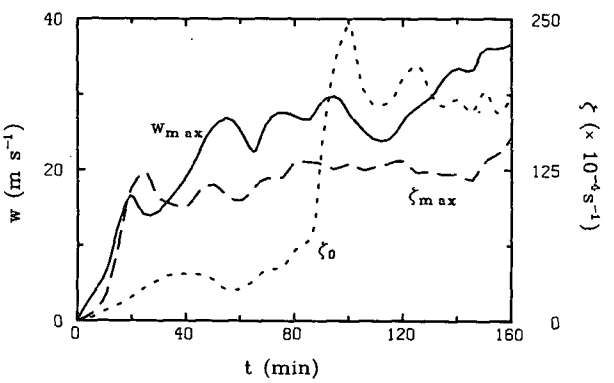

FIG. 2. Maximum vertical velocity (solid line), maximum vertical vorticity at middle levels (dashed line), and maximum vertical vorticity at the lowest grid level (dotted line) vs time.

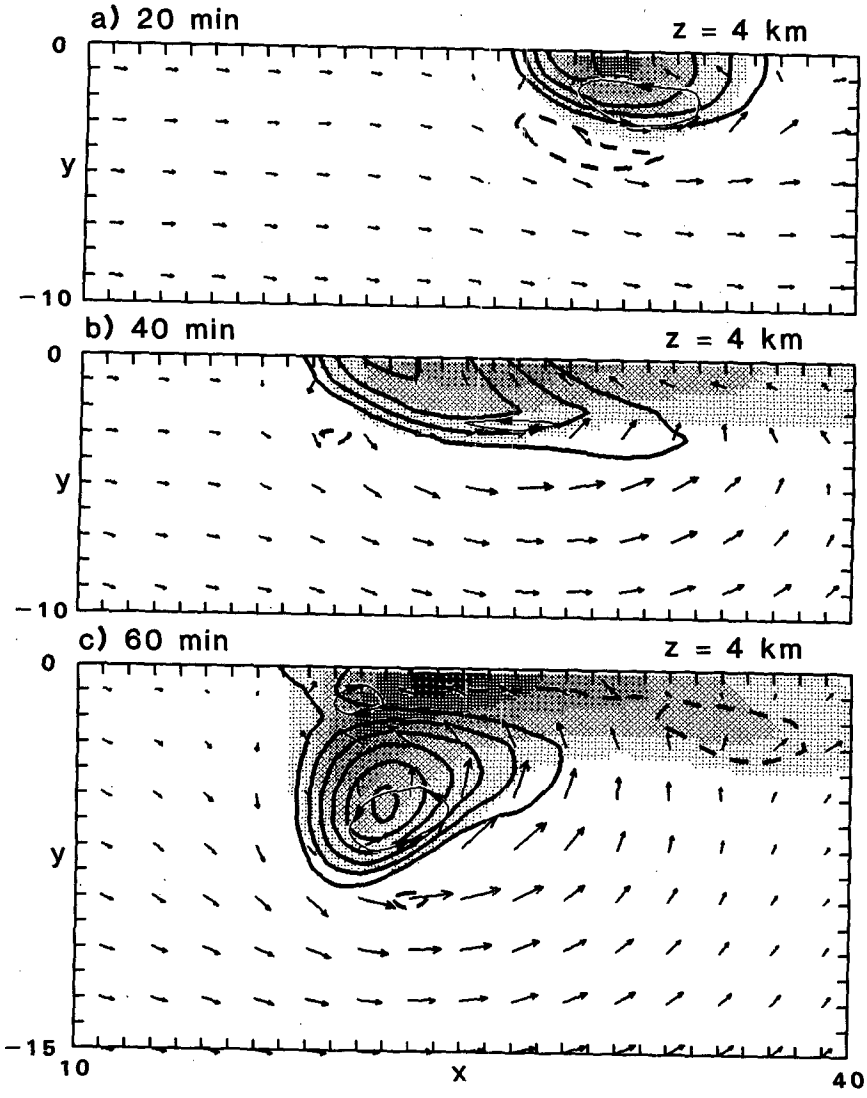

FIG. 3. Time sequence depicting the development of the initial cell at $z = 4$ km. The vertical velocity (the contour lines are in intervals of 3 m s^{-1}; dashed lines indicate negative values; zero lines are omitted), the horizontal wind vectors (one grid length = 10 m s^{-1} plotted at every other grid point; true for all subsequent plots, unless specified otherwise), the rainwater field (shaded in 2 g kg^{-1} increments beginning with the 1 g kg^{-1} value; true for all subsequent plots) and the vertical vorticity (thin line enclosing the positive and negative areas greater in magnitude than 0.01 s^{-1} with arrows indicating the sense of the rotation) are displayed at t = 20, 40, and 60 min over the indicated portion (labeled in kilometers) of the computational domain.

southward with time. Note that the maximum updraft at this level lies along the cold-air boundary. That is, at this level, the updraft is composed of both the warm air from the south and the cool air from the north, the latter originating aloft. We shall demonstrate that this feature is crucial to the development of low-level rotation.

Returning to Fig. 2 we note a quasi-steady updraft over the period t = 60–95 min. Figure 5a displays the relevant features of the flow at t = 90 min which is representative of this period. At the lower level there is a pattern of flow that has become familiar to observers of severe thunderstorms (e.g., Barnes, 1978; Golden and Purcell, 1978; Lemon and Doswell, 1979). The main area of updraft extends south-southwestward while the wind vectors indicate strong convergence along the cold-air boundary (known as the "gust front"). The area of most intense rain and downdraft is generally to the northwest. Rotation is strong and, at this time, is most intense at the updraft center as evidenced by the "v" indicating the location of maximum vertical vorticity. The appendage of

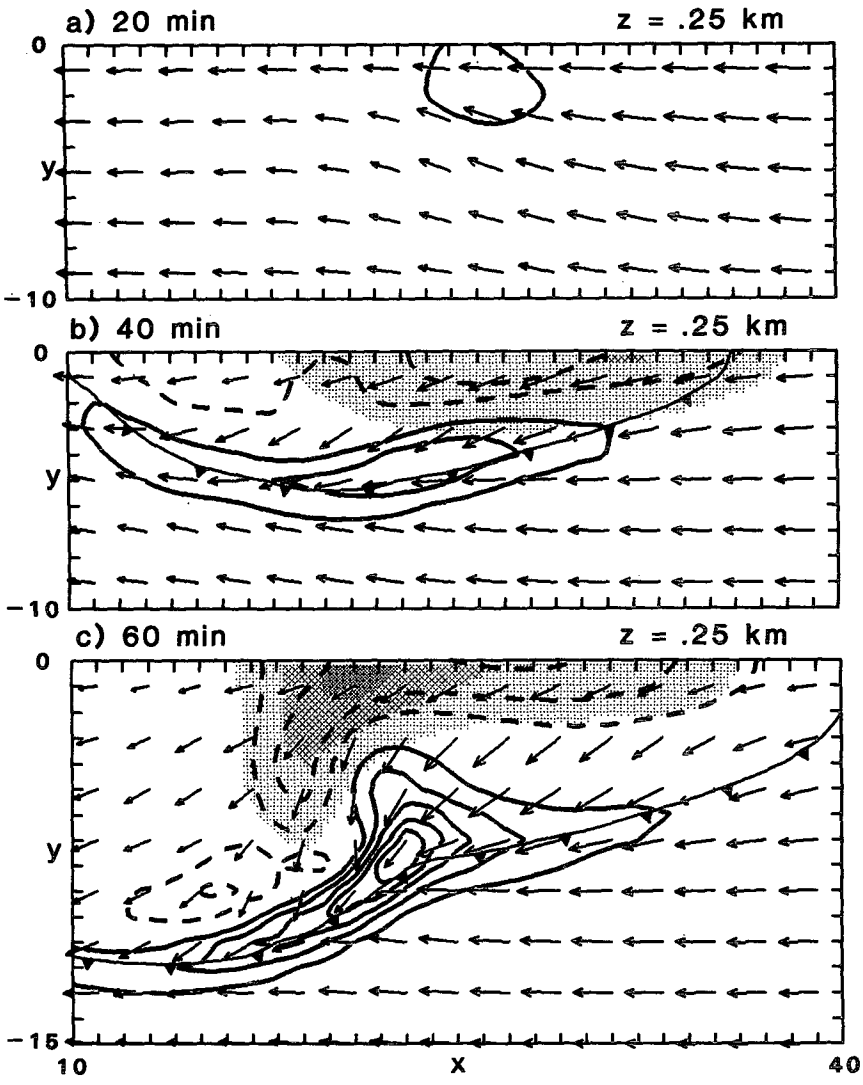

FIG. 4. Time sequence depicting the development of the low-level flow. The vertical velocity (contour interval = 0.5 m s^{-1}), the horizontal wind vectors and the rainwater field are displayed at t = 20, 40, and 60 min over the same regions as in Fig. 3. The position of the −1°C perturbation isotherm is depicted as a cold front on a synoptic chart.

rainwater extending around the southwest side of the updraft has been identified by WK as the model equivalent of the "hook echo" which is commonly detected by radar. Again, note that the cold-air boundary nearly coincides with the maximum updraft at this level. At z = 4 km, there is, as in Fig. 3c, a cyclonically rotating updraft with an anticyclonically rotating downdraft to the north. The rainwater field evinces the hook shape on the west side of the updraft, and on the left–forward side there is a feature (more clearly seen at the later times) that Weisman and Klemp (1982) identified as the model equivalent to the "v-notch" commonly observed in the reflectivity at middle levels in a supercell (Lemon, 1980).

Of course, the foregoing contour plots represent only a tiny fraction of the information contained in the model data. To get a more fully integrated view of the simulated storm, we present in Fig. 6 three-dimensional contour plots of cloudwater (>0.1 g kg^{-1}) and rainwater (>0.5 g kg^{-1}) viewed from the southeast. The cloudwater field shows the main column of cloud associated with the main updraft, a "flanking line" (Lemon, 1976) of clouds extending to the southwest, and a lowering of the cloud base just below the main updraft (we identify this feature as the "wall cloud" in Section 5). The rainwater field exhibits a hollow cavelike structure which Klemp *et al.* (1981) have identified as the weak-echo region, bordered by the model equivalent hook echo at low levels.

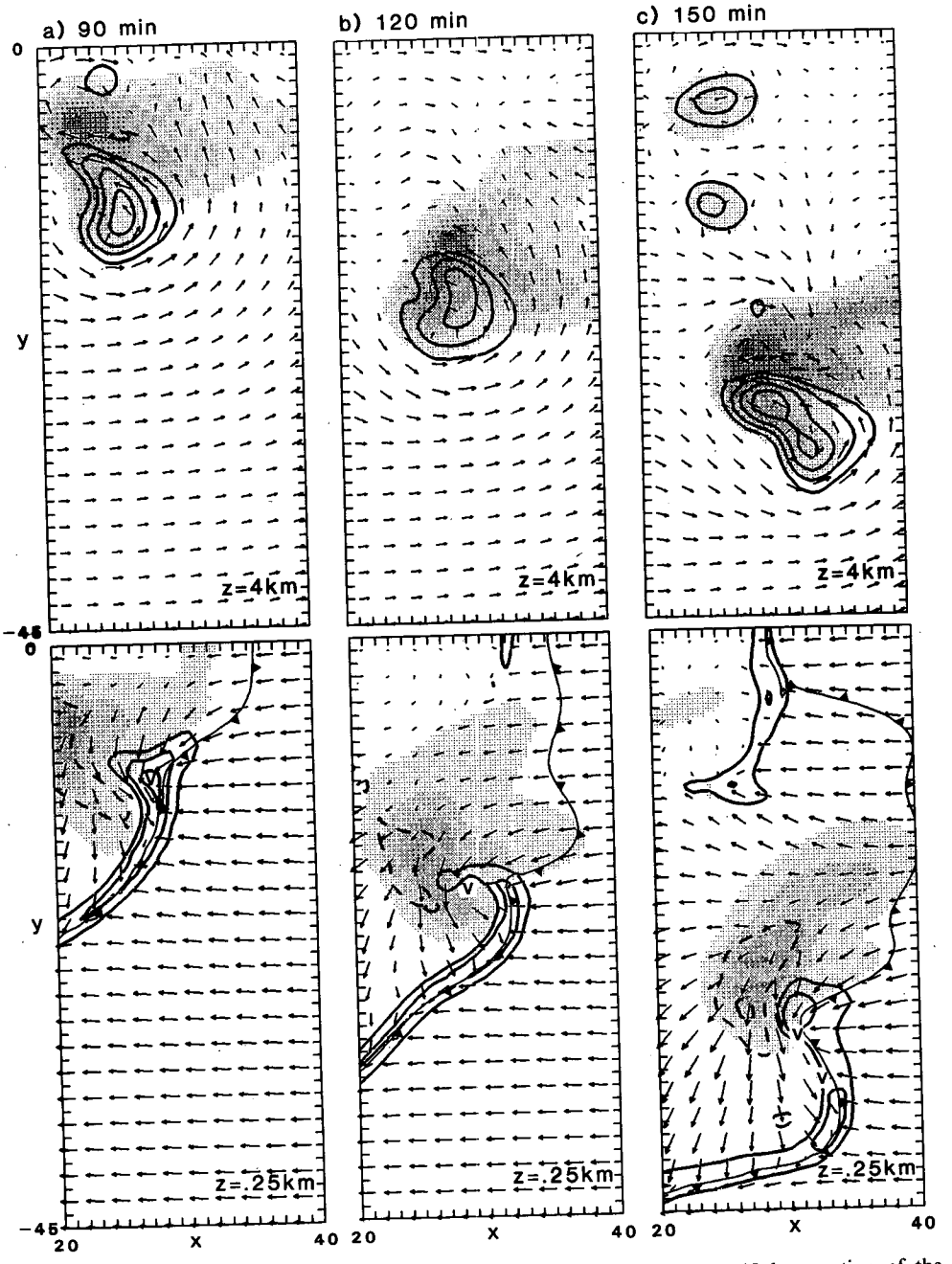

FIG. 5. Time sequence of the flow at $z = 4$ and 0.25 km over a 20 × 45 km portion of the computational domain at (a) 90 min, (b) 120 min, and (c) 150 min. The contour interval for w is 5 m s^{-1} at $z = 4$ km and is 1 m s^{-1} at 0.25 km with the zero lines omitted. The wind vectors, rainwater shading, and the thunderstorm outflow boundary are represented as in Figs. 3 and 4. The locations of the low-level maxima of vertical vorticity are indicated by the "v".

Figure 5b displays the same information as Fig. 5a but for $t = 120$ min; except for the southward propagation, the solution at $z = 4$ km is not much different, but at $z = 0.25$ km the structure has changed radically. The updraft has become highly contorted and the gust front has occluded. A sharp drop in updraft strength (Fig. 2) occurs between $t = 95$–120 min in association with this occlusion. The maximum vorticity has shifted from the updraft's center to the gradient between the updraft and downdraft (but within the updraft). This sequence of events is typical of those observed as a thunderstorm enters its tornadic phase (e.g., Lemon and Doswell, 1979; Klemp and Rotunno, 1983). Klemp and Rotunno

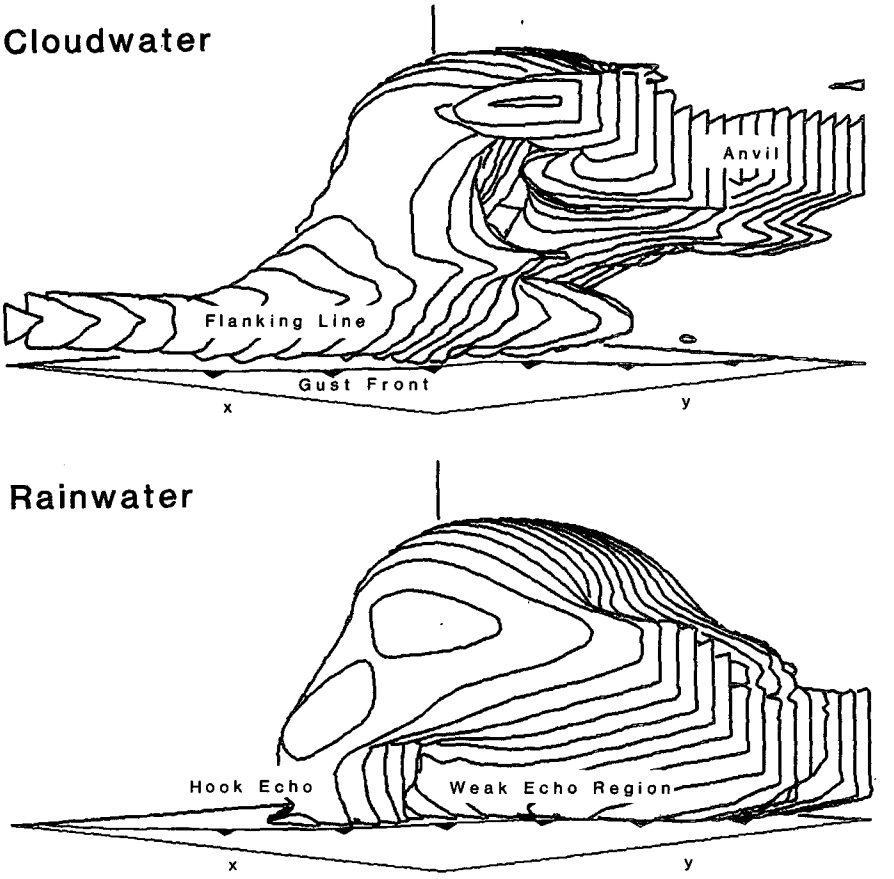

FIG. 6. Three-dimensional contour representations of the cloudwater (>0.1 g kg^{-1}) and rainwater (>0.5 g kg^{-1}) at t = 90 min on a 24 × 24 km portion of the computational domain. The view is to the northwest and features are noted which we believe are the model equivalent to the "flanking line," "anvil," "weak-echo region," "hook echo," and "gust front." The cold frontal boundary again depicts the location of the −1°C perturbation isotherm.

(1983) argue that the transition takes place when the low-level rotation exceeds the midlevel rotation. It is then that the cyclostrophic pressure drop is greater at lower levels than it is at middle levels and so an adverse pressure gradient retards the updraft at its center. This is essentially the "vortex valve" effect invoked by Lemon *et al.* (1975) to explain the observed decline in updraft strength as low-level rotation increased in the Union City, OK storm. Figure 2 shows that the present simulation is consistent with these ideas: the low-level vorticity exceeds the midlevel vorticity just before the transition occurs.

The overall development shown in Fig. 2 is qualitatively similar to that observed by Burgess (1974; his Fig. 11a). In that case the supercell became a squall line after it collapsed; however, in many cases the supercell reintensifies (Burgess *et al.*, 1982). Such is the case in the present simulation; the storm reaches a quasi-steady configuration similar to that shown at t = 150 min in Fig. 5c and propagates in a more or less continuous fashion to the right of the mean wind over the last 40 min of integration. Note in Fig. 5c that new updrafts have appeared to the north along the residual cold air pool left behind by the supercell. This sort of development has been discussed before by Wilhelmson and Klemp (1981) in their simulation of the splitting thunderstorms which developed in nearly unidirectional shear near Fort Sill, OK on 3 April 1964 (see also Weisman and Klemp, 1982). Being somewhat outside the present focal point, these updrafts will not be discussed here.

3. Rotation in the supercell

Even a cursory examination of the wind vectors in the foregoing figures leads to the conclusion that there is an organized "rotation" present. However, an exact, unambiguous measure of this property remains elusive. The measure of rotation used most often is the vorticity, but this by itself is limited because the vorticity represents only the local and instantaneous rate of rotation of the medium (e.g., Truesdell, 1954, p. 66). For example, a two-dimensional shear layer has vorticity but is obviously a

much different kind of flow than, say, the one in Fig. 5a. But vorticity does have one feature that favors its use as a diagnostic tool: we know and understand its governing equation. Further, if a distribution of vorticity is two-dimensional (rather than one-dimensional as it is in the shear layer example), then the associated streamlines curve around local extrema of vorticity. With these caveats, we assert that an explanation of how vorticity becomes large and concentrated is tantamount to an explanation of the rotation observed in simulated thunderstorms.

The equation governing the vorticity is, to the inviscid Boussinesq approximation,

$$\frac{\partial \boldsymbol{\omega}}{\partial t} = -\mathbf{v}\cdot\nabla\boldsymbol{\omega} + \boldsymbol{\omega}\cdot\nabla\mathbf{v} + \nabla\times(B\mathbf{k}), \tag{1}$$

where $\boldsymbol{\omega} = (\xi, \eta, \zeta)$, $\mathbf{v} = (u, v, w)$ and B are the vorticity, velocity, and buoyancy, respectively; t is time; $\nabla = \partial/\partial x\mathbf{i} + \partial/\partial y\mathbf{j} + \partial/\partial z\mathbf{k}$; x, y, and z are positive eastward, northward, and upward, respectively, and $\mathbf{i}$, $\mathbf{j}$, and $\mathbf{k}$ are the respective unit vectors in the x, y, and z directions. The terms on the right-hand side represent, respectively, the change of vorticity at a point due to advection, the change in orientation and length of vortex tubes, and baroclinic generation. Because the rotation about a vertical axis is an important distinguishing feature of supercell thunderstorms, the vertical component of Eq. (1) has been the subject of much study in this connection. It is

$$\frac{\partial \zeta}{\partial t} = -\mathbf{v}\cdot\nabla\zeta + \boldsymbol{\omega}_H\cdot\nabla_H w + \zeta\frac{\partial w}{\partial z}, \tag{2}$$

where the terms on the right are referred to, according to convention, as the advection, tilting, and stretching terms, respectively. The subscript H denotes the horizontal component of a vector. In our analysis of the vorticity equation we found that frictional effects are not very important; hence, they are not included in Eq. (1).

a. Rotation at midlevels

In almost all of the three-dimensional cloud-modeling studies to date, the initial state contains no vertical component of vorticity (hereinafter we say "vertical vorticity" and likewise for the other components). The numerical simulations indicate the development of vertical vorticity immediately after the vertical motion begins. Figure 3a (see also Fig. 14 of WK) shows cyclonic rotation on the south flank of the initial updraft. At a later stage (Fig. 3b), the updraft weakens at its center as the initial cell begins to split and the cyclonic rotation weakens on the north flank of the southern member of the split pair. Then (Fig. 3c), anticyclonic rotation develops on the north flank as the updraft weakens to the point of becoming downdraft; the updraft begins to propagate southward and nearly comes into phase with the positive vertical vorticity.

A simple model for this evolution of the vertical vorticity can be obtained by linearizing Eq. (2) about the environmental wind (Rotunno, 1981);

$$\frac{D\zeta}{Dt} = \bar{\boldsymbol{\omega}}_H\cdot\nabla_H w, \tag{3}$$

where $D/Dt = \partial/\partial t + U\partial/\partial x$ and $\bar{\boldsymbol{\omega}}_H\cdot\nabla_H w = \partial U/\partial z\cdot\partial w/\partial y$ in the present case. Because here $\partial U/\partial z > 0$, Eq. (3) predicts that positive (negative) vertical vorticity should be generated on the updraft's south (north) flank where $\partial w/\partial y$ is positive (negative). The interpretation is that the horizontal vortex lines associated with the environmental shear flow are tilted upward on the south flank and downward on the north flank by the developing updraft. When the updraft weakens at its center, $\partial w/\partial y$ changes sign on the north flank of the southern member of the split pair; according to Eq. (3) negative vertical vorticity is produced by the downward bending of the environmental vortex lines (see also Bluestein and Sohl, 1979). As a downdraft develops on the center axis, two updraft–downdraft systems begin to propagate northward and southward, respectively. The southward (northward)-traveling system has a cyclonically (anticyclonically) rotating updraft and an anticyclonically (cyclonically) rotating downdraft.

To see how this follows from Eq. (3) and to develop a relation we will need later, we define

$$\frac{Dh}{Dt} = w, \tag{4}$$

where h is the vertical displacement field. Substituting Eq. (4) into Eq. (3), then integrating (assuming a nongrowing disturbance) yields

$$\zeta = \bar{\boldsymbol{\omega}}_H\cdot\nabla_H h \tag{5}$$

(Davies-Jones, 1983). An updraft–downdraft pair can be represented by a hill in the displacement field propagating to the south; the vortex lines of the mean shear flow lie on its surface and point toward the north (in the present case). The vortex lines tilt upward on the hill's south side and downward on its north side. Since the vertical velocity should also be positive on the south side of the hill and negative on the north, it is clear that, under the stated conditions, the linear theory predicts that an updraft will have positive vertical vorticity and a downdraft negative vorticity as the system propagates to the right of the mean shear (see Fig. 3 of Davies-Jones, 1983; Fig. 3b of Rotunno, 1981; or Fig. 2 of Lilly, 1982).

We propose a more comprehensive model of thunderstorm rotation based on the conservation of equivalent potential vorticity. Since the equivalent potential temperature θ_e is nearly conserved, there is a near one-to-one correspondence between θ_e and B, and

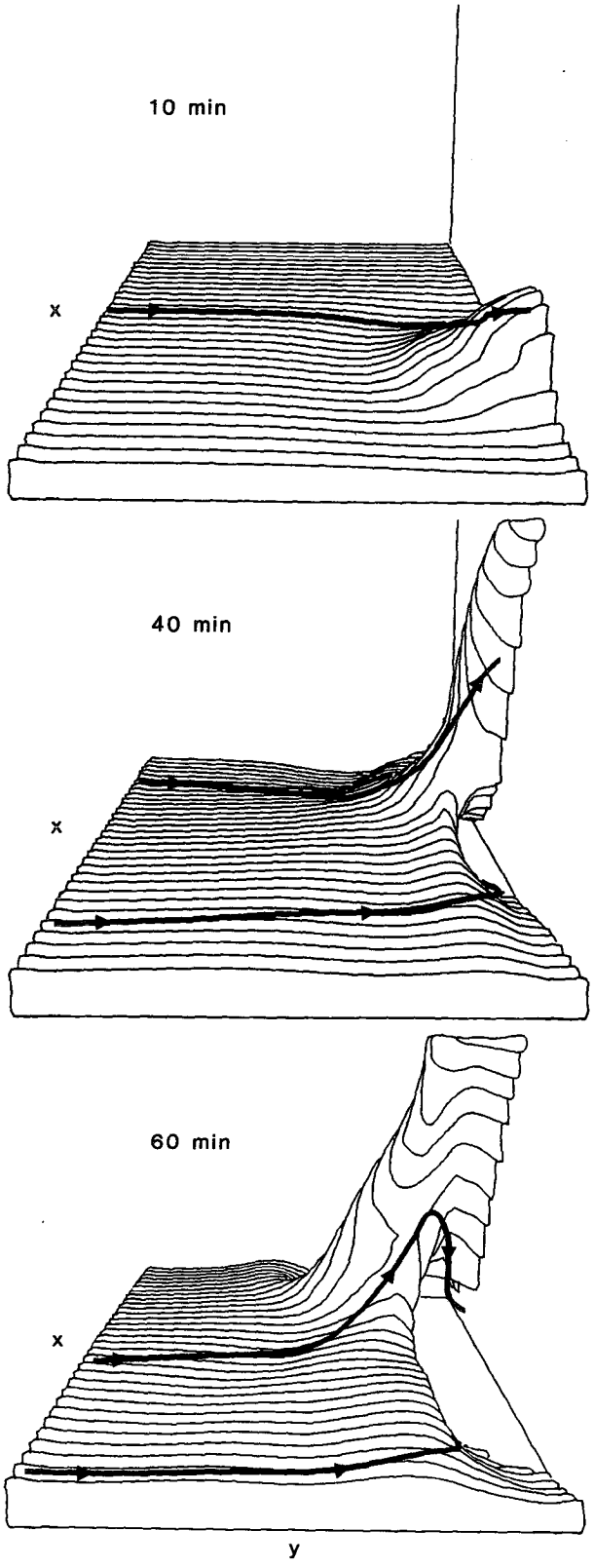

FIG. 7. Three-dimensional perspective (the view is westward) showing the contour θ_e = 336 K surface on a 30 × 20 × 9 km portion of the computational domain. The upward surging of the high-θ_e air reflects the updraft region. Vortex lines, denoted by heavy solid lines, lie approximately on the constant-θ_e surface owing to near conservation of the initially zero equivalent potential vorticity in the model. These vortex lines tilt upward on the south flank, producing a positive vertical component of the vorticity vector. As the updraft propagates to the south, low-θ_e air descends on the north flank. The vortex lines, adhering to the surface, tilt downward, producing a negative component of the vorticity vector on the north flank. The vertical scale is exaggerated by a factor of 2.

diffusion of vorticity is not significant; it follows from Ertel's theorem (see Appendix A) that

$$\frac{d}{dt}\left(\frac{\omega \cdot \nabla\theta_e}{\bar{\rho}}\right) = 0, \tag{6}$$

where $\bar{\rho}(z)$ is the base-state density and the quantity in brackets is termed the "equivalent potential vorticity." In our initial state $\omega \cdot \nabla\theta_e = 0$, and by Eq. (6) it must remain so; geometrically speaking, this means that *a vortex line must lie in a surface of constant-θ_e*.

A sequence of three-dimensional contour plots of constant-θ_e surfaces and a few vortex lines which illustrate the foregoing remarks are displayed in Fig. 7. Since the initial state has no horizontal variations of θ_e (except for the small one associated with the initial thermal), the vortex lines are all horizontal. In the first stage (t = 10 min) the high-θ_e air is transported upward and so are the vortex lines, which are constrained to lie in their initial-θ_e surface. Hence there is positive vertical vorticity on the south flank and negative on the north (not shown). As the updraft propagates southwards, the environmental vortex lines are continually lifted upward on the south side. The cyclonic rotation of the updraft at these middle levels acts to bring the low-θ_e air from midlevels on the storm's south side around the east side to the north side where, encountering precipitation, evaporation renders the air negatively buoyant, thereby inducing its descent. This is reflected at t = 40 and 60 min as a depression in the constant-θ_e surface on the north side. The environmental vortex line lying on this surface that tilts upward on the south flank of the updraft must tilt downward on the north flank. Hence, the flow on the north flank of the southern member of the split pair must have negative vertical vorticity. As the updraft maximum propagates toward the place where the positive vertical vorticity is being produced (the south flank of the updraft), there is, therefore, a tendency for the vertical velocity and vorticity to come into phase. Alternatively, moving to the south in the updraft's frame of reference, one would observe winds from the south, which bring positive vertical vorticity from the updraft's south flank where it is being produced, towards its center. Similar remarks apply to the downdraft. At t = 40 and 60 min, vortex lines (shown in the foreground) which run from south to north turn toward the southwest, and then curl under and go out of view.

This shows the environmental vorticity joining with the baroclinically produced vorticity along the gust front. We will return to this point in the discussion of the low-level rotation.

Significantly, in this case of zero equivalent potential vorticity, one can show that

$$\zeta = \omega_H \cdot \nabla_H h, \tag{7}$$

where h is the height of a surface of constant-θ_e. This relationship provides the nonlinear extension of the linear result embodied in Eq. (5) and clarifies the linear theory appearing to work well in spite of the fact that its assumptions are violated. Within the updraft, nonlinear effects are significant as vertical advection turns the constant-θ_e surfaces toward the vertical and baroclinic generation of horizontal vorticity acts to modify the ambient vorticity of the shear flow. However, along the outer edges of the storm, the constant-θ_e surfaces approximate a hill and the horizontal vorticity is approximately that of the environment. It is here that the linear results apply and explain the salient feature of the phenomenon. The foregoing nonlinear theory substantially strengthens and extends the linear prediction that an updraft should rotate cyclonically if it propagates to the right of the shear.

b. *Rotation at low levels*

The theory for storm rotation at low levels is more complicated than the theory for storm rotation at middle levels. For this reason, we proceed here more deliberately with a study of the vertical vorticity budget before we interpret the results in terms of equivalent potential vorticity and circulation.

The distribution of ζ and the stretching and tilting terms at $z = 0.25$ km at $t = 90$ min (see Fig. 5a) are shown in Figs. 8a–c, along with the trajectory of the air parcel passing through the point of maximum

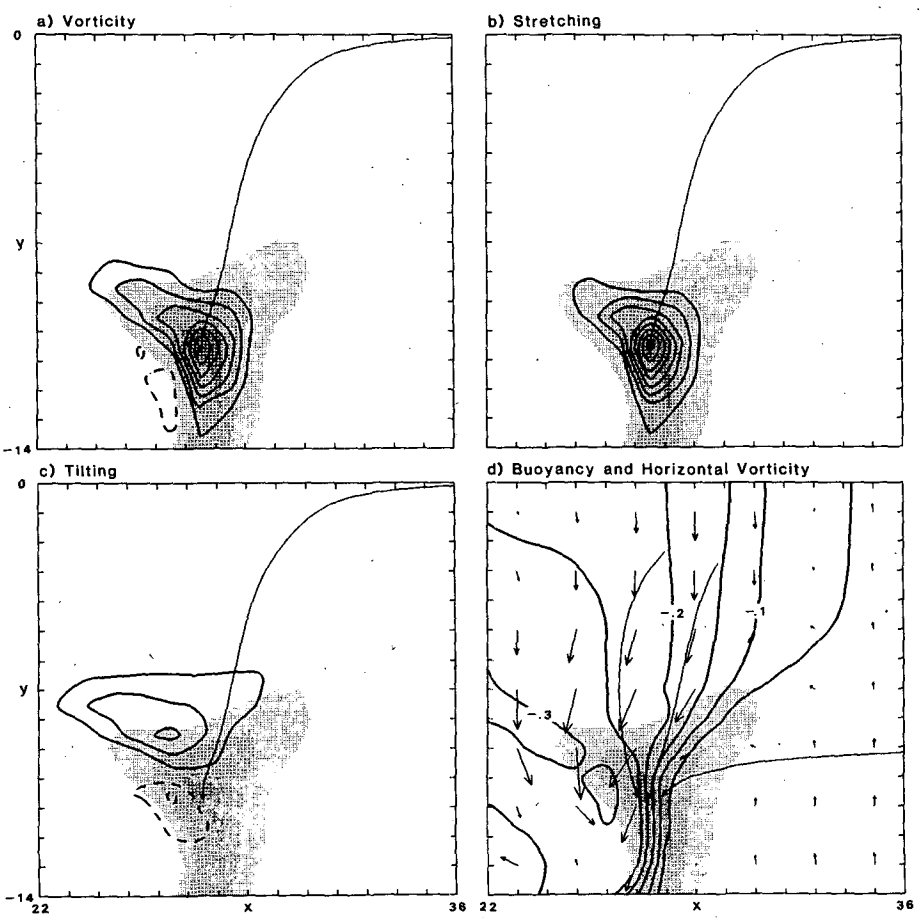

FIG. 8. (a) Vertical vorticity (contour interval = 0.002 s^{-1}); (b) stretching (contour interval = 2 $\times 10^{-5}$ s^{-2}); (c) tilting (contour interval = 10^{-5} s^{-2}); and (d) the horizontal vorticity vectors (placed every other grid point with one grid length = 0.015 s^{-1}) and buoyancy (contour interval = 0.05 m s^{-2}) at $t = 90$ min at $z = 0.25$ km. The trajectory of the air parcel located at the position of maximum vertical vorticity is indicated in (a)–(c). In (d), ten-minute segments of three neighboring parcels are shown, with the center segment corresponding to that shown in (a)–(c). The updraft is shaded in increments of 1 m s^{-1}, beginning with the 1 m s^{-1} value.

vertical vorticity. The air parcel, entering from the northeast, encounters weak positive tilting and subsequently strong stretching, and thereby acquires the large value indicated in Fig. 8a. The relative weakness of the tilting with respect to the stretching does not mean that tilting is unimportant. Since the model is initiated with zero vertical vorticity in the environment, all air parcels entering the updraft from the environment have zero vertical vorticity, and no amount of stretching can change this unless there is some tilting to provide the vertical vorticity to be stretched.

The distribution of the tilting term (Fig. 8c) is the first hint that the mechanism whereby the low-level updraft acquires rotation is very different from that of the midlevel updraft. Here, the maximum positive values are on the left (north) flank of the updraft with negative values on the right—precisely the opposite of what the tilting of the environmental horizontal vorticity would give. To see why this is so, we will take a closer look at the tilting term of Eq. (2). This term, being the dot product of the horizontal component of the vorticity with the horizontal gradient of the vertical velocity, is positive if the two vectors point in the same direction. Figure 8d contains the horizontal vorticity vectors together with shaded contours of vertical velocity at $z = 0.25$ km. In the southeast sector of the flow the horizontal vorticity is that of the environmental shear; it is relatively small and is directed northward. However, as shown in Fig. 8c, the dominant positive tilting takes place to the north of the updraft maximum. There, the horizontal vorticity vectors are significantly larger and point toward the south to southwest, and so point up the horizontal gradient of vertical velocity. The buoyancy field in Fig. 8d shows that this large horizontal vorticity is due to baroclinic generation along the low-level cold air boundary (Klemp and Rotunno, 1983) through the third term on the right-hand side of Eq. (1).

Two other trajectories (10 min segments) are shown in Fig. 8d—one terminating 0.5 km to the east of the maximum vertical vorticity, the other terminating 0.5 km to the west. Analysis of the history of these parcels indicates that the parcel on the west side originates at middle levels (4 km), the parcel on the east side originates at low levels and the one in between originates at 3.4 km. Thus, as the air approaches from the northeast, it first acquires horizontal vorticity directed toward the southwest from baroclinic generation along the cold air boundary. This horizontal vorticity is then tilted upward to produce cyclonic vertical vorticity as the air encounters the updraft. Finally, the air is subjected to intense stretching whereby the vertical vorticity may increase exponentially (following a parcel). Although the trajectory passing through the maximum vertical vorticity at $z = 250$ m originated at 3.4 km above the ground, it has descended to 700 m by the time it enters the domain shown in Fig. 8. Thus, the baroclinic vorticity generation clearly occurs at low levels as the flow approaches the updraft.

One can also view the development of low-level rotation in terms of the conservation of the (zero) equivalent potential vorticity. A three-dimensional contour plot of the $\theta_e = 331$ K contour, which encloses all values of θ_e *less* than that amount, and the vortex line passing through the location of maximum vertical vorticity at $t = 90$ min are shown in Fig. 9. The vortex line enters from the south (consistent with the environmental vorticity) but then turns toward the southwest as it meets the cold air boundary because it cannot enter the low-θ_e air. We include this discussion here mainly for completeness; an analysis solely in terms of equivalent potential vorticity would, in this case, be much less illuminating than the preceding vorticity analysis because equivalent potential vorticity analysis alone does not illustrate the essential role of the baroclinic mechanism as clearly.

Yet this is not the entire story. As already mentioned, the air just to the east of the vorticity maximum originates at low levels, but the air just to the west is cold, low-θ_e air which originates aloft. Both streams are then drawn together into the low-level updraft. The foregoing analysis, which is purely in terms of vorticity, does not give this two-stream view its proper weight. In order to emphasize the latter, we have analyzed the circulation of a fluid curve surrounding the location of maximum vertical vorticity.

The circulation $C(t)$ is defined as

$$C(t) = \oint \mathbf{v} \cdot d\mathbf{l}, \tag{8}$$

where the integration is performed around a closed material curve (see, e.g., Batchelor, 1967, p. 273). The equation governing the change in circulation following the material curve is, to the inviscid Boussinesq approximation,

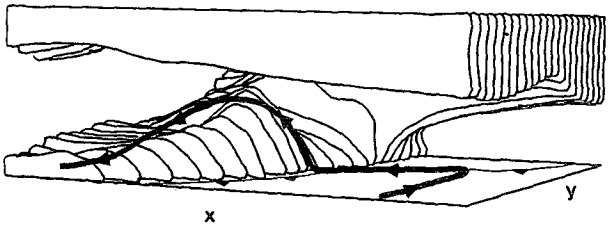

FIG. 9. Three-dimensional perspective (looking to the northwest) of the surface which encloses all values of θ_e below 331 K, together with the vortex line (heavy line) which passes through the location of maximum vertical vorticity at $t = 90$ min on a $14 \times 14 \times 4$ km portion of the computational domain. The vertical scale is exaggerated by a factor of 2. The cold frontal boundary indicates the location of the -1°C perturbation surface isotherm.

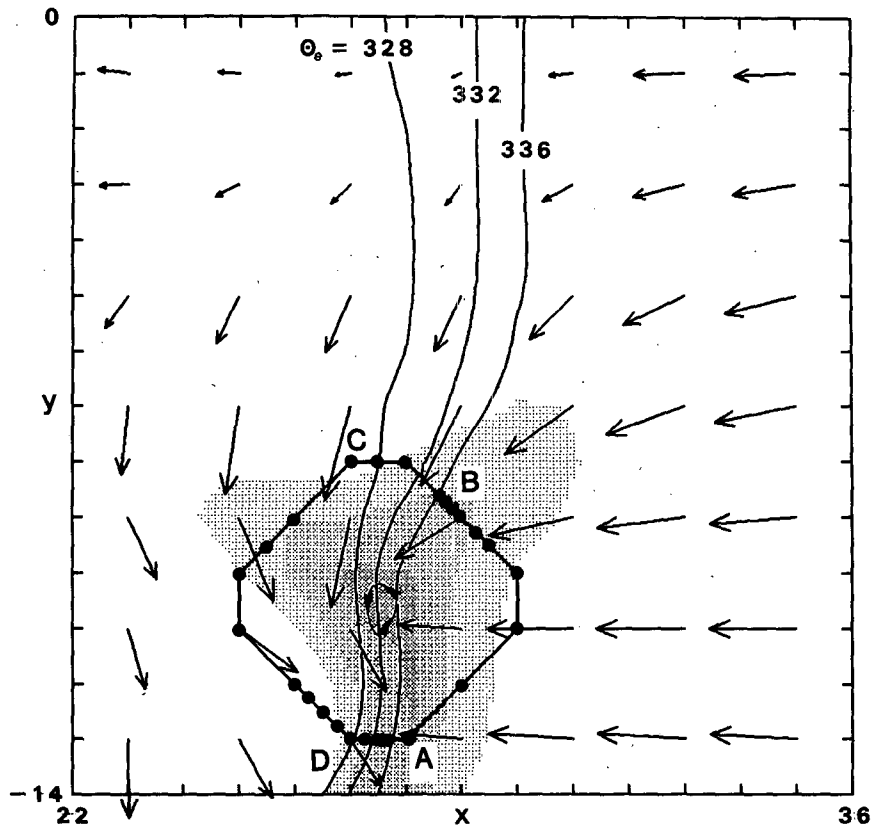

FIG. 10. A material curve surrounding the location of maximum vertical vorticity and the horizontal wind vectors at t = 90 min and z = 0.25 km. There are 39 points on the curve which are followed backward in time so that the evolution of the material curve may be studied. The updraft is shaded in increments of 1 m s^{-1} beginning with the 1 m s^{-1} value. The position of maximum vertical vorticity is indicated by the ζ = 0.013 s^{-1} closed contour with the arrows. θ_e contours in the vicinity of the maximum vertical vorticity are also included, labeled in K.

$$\frac{dC}{dt} = \oint B\mathbf{k}\cdot d\mathbf{l}. \tag{9}$$

(V. Bjerknes' first circulation theorem; cf., Eliassen and Kleinschmidt, 1957, p. 14). We mark out the material curve shown in Fig. 10 for study. This curve has the location of maximum vertical vorticity at its center and cuts across the cold-air boundary. From the preceding discussion, we know that the vertical vorticity maximum must lie at the cold air (more precisely, low-θ_e) boundary; since all vortex lines lie in a constant-θ_e surface, there can be no circulation around any curve lying wholly on such a surface. Hence a material curve with nonzero circulation must cut across constant-θ_e surfaces.

Although the basic numerical simulation was performed on a CRAY-1 computer, history files were created after every 5 min of integration and were then put on a VAX 11/780 minicomputer for further analysis. The Lagrangian calculation we describe here was greatly facilitated by this procedure; a point is identified and, by a process of interpolation through space and time, its trajectory computed. We identified 39 such points (shown in Fig. 10) and calculated the paths that they took to reach their present location. Using this number of points allowed us to identify the neighboring points of any one point sufficiently to keep track of the material curve. The results of this calculation are displayed in a three-dimensional perspective in Fig. 11. Here the view is to the north, and the evolution of the curve is displayed over the 15 min just prior to t = 90 min. Following the curve from t = 75 min onward shows that the curve shrinks (i.e., there is convergence) and that the part of the curve lying on the southeast side (DAB) stays close to the ground, whereas the part of the curve on the northwest side (BCD) originates from higher levels within the thunderstorm. Carrying the calculation further back in time is uninformative for two reasons. First the material line segment BCD becomes highly contorted as it is traced back into the thunderstorm. Second, and more important, is that the circuit obtains its positive circulation over this 15 min period. As shown in Fig. 12, on the material curve

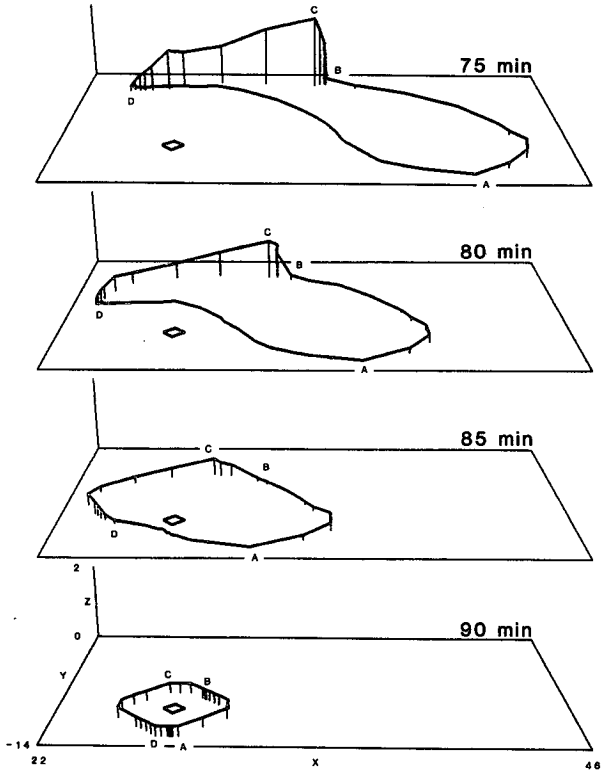

FIG. 11. A time sequence of perspective plots (looking to the north) which show the three-dimensional evolution, in 5 min intervals, of the material curve shown in Fig. 10 on a 24 × 14 × 2 km portion of the computational domain. The locations of points A–D are shown at each time for reference.

in question the circulation actually is negative at t = 65 min but increases thereafter. The term on the right-hand side of Eq. (9) (also calculated from the model data), which shows the circulation is produced by buoyancy effects, is also shown in Fig. 12. The circulation that would be produced by the computed buoyancy term can be estimated from Fig. 12 as 0.5 × (200 m^2 s^{-2}) × (1500 s) ≈ 1.5 × 10^5 m^2 s^{-1}. The actual increase in circulation over this period is approximately 1.2 × 10^5 m^2 s^{-1}. We attribute the discrepancy to frictional effects which have been ignored because they are difficult to calculate and because the present results are good enough to endorse the qualitative arguments given here.

How does this happen and how does it relate to our explanation for the generation of low-level vorticity? The material curve at t = 75 min together with the buoyancy field in the three-dimensional perspective used in Fig. 11 is displayed in Fig. 13. Consider the integral of B along this circuit [see Eq. (9)]: along DAB it is zero because dz = 0; along BC it is slightly negative because B is slightly negative and dz is positive; along CD it is strongly positive because B is strongly negative and dz is negative. So we conclude that there is positive circulation around the material curve in question: part of it passed through the cold air in a manner that created the positive circulation.

The relation of this argument to the vorticity argument is straightforward. Transforming the right-hand side of Eq. (9) using Stokes' theorem gives

$$\frac{dC}{dt} = \oint\!\!\oint \nabla \times (B\mathbf{k}) \cdot d\mathbf{A}$$

$$= \oint\!\!\oint \left(\frac{\partial B}{\partial y} dA_x - \frac{\partial B}{\partial x} dA_y \right), \qquad (10)$$

where the integration is over any (sufficiently well behaved) area bounded by the material curve. The integrand is the baroclinic production of vorticity term of Eq. (1). Imagining an elastic membrane stretched over the curve ABCDA in Fig. 13 we find that over that portion of the membrane enclosed by the segment DABD, $dA_x \approx dA_y \approx 0$, and over that portion of the membrane enclosed by the segment BCDB, $dA_x \approx 0$ and $dA_y < 0$. Over the segment BCDB, $\partial B/\partial x > 0$ at the cold air boundary (particularly at low levels) and, so, the integral is positive. This integral over BCDB is just the pointwise sum of all the vorticity being generated along that surface according to Eq. (1). Thus, contributions to the circulation are equated with the contributions to the vorticity in all of the air parcels passing through that surface. Both the vorticity and circulation viewpoints must lead to the same answer; the foregoing discussion merely shows how.

4. Supercell propagation

Our simulated supercell has the remarkable property of propagating to the south with little change in form as long as we carry out the integration. The southward propagation in the velocity fields at t = 90, 120 and 150 min at z = 4 km and 0.25 km is shown in Fig. 5. At z = 4 km, the updraft propa-

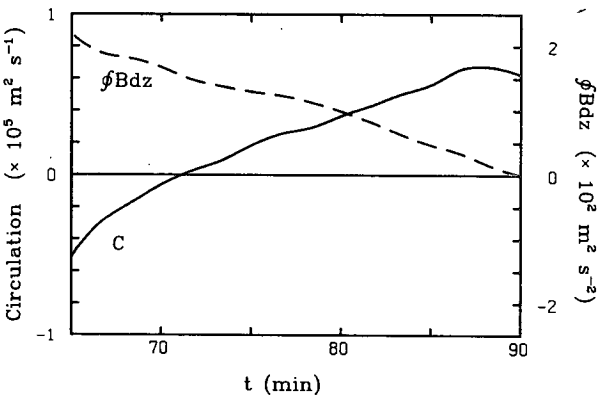

FIG. 12. The circulation and generation of circulation computed around the material curve shown in Fig. 11, vs time.

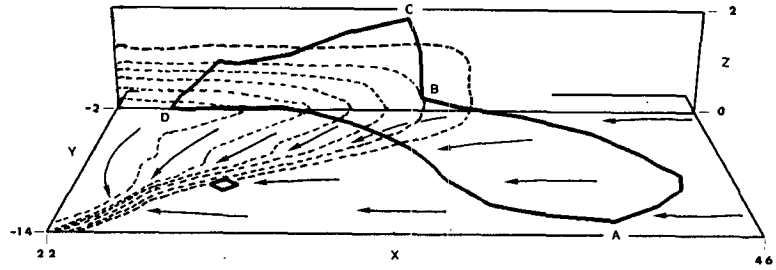

FIG. 13. An illustration of how the baroclinic generation is positive as the curve evolves. The surface buoyancy field and the buoyancy fields in the $y = -2$ km plane are displayed together with the material curve at $t = 75$ min. This display is chosen because the curve at this time has two primary branches: DAB, which lies close to $z = 0$, and BCD, which stands nearly along the $y = -2$ km plane. The surface flow at this time is indicated by arrows.

gates to the south at approximately 4 m s^{-1}, while at $z = 0.25$ km the updraft, in addition to its southward propagation, undergoes a dramatic change in shape between $t = 90$ and 120 min. Thereafter, the low-level updraft more or less retains the curved "horseshoe" shape that it acquired in the transition.

We need to determine, then, the reason that the updraft changes its location as time passes. We seek the answer to this question from the vertical component of the momentum equation, which, to the inviscid Boussinesq approximation, is

$$\frac{\partial w}{\partial t} = -\mathbf{v}\cdot\nabla w - c_p\bar{\theta}\frac{\partial \pi}{\partial z} + B, \tag{11}$$

where the three terms on the right-hand side represent changes of vertical velocity at a point due to advection, the vertical pressure gradient, and buoyancy, respectively. To better understand the nature of the pressure-gradient term, we take the divergence of the vector momentum equations used in our cloud model together with the anelastic continuity equation, $\nabla\cdot(\bar{\rho}\mathbf{v}) = 0$, to obtain

$$-\nabla\cdot(c_p\bar{\rho}\bar{\theta}\nabla\pi) = \nabla\cdot(\rho\mathbf{v}\cdot\nabla\mathbf{v}) - \partial B/\partial z \tag{12}$$

(Klemp and Rotunno, 1983). Following Rotunno and Klemp (1982) we consider the contribution to π from the terms involving velocity derivatives and from the buoyancy by letting $\pi = \pi_{dn} + \pi_b$, and solving the two Poisson equations

$$\nabla\cdot(c_p\bar{\rho}\bar{\theta}\nabla\pi_{dn}) = -\nabla\cdot(\bar{\rho}\mathbf{v}\cdot\nabla\mathbf{v}), \tag{13a}$$

$$\nabla\cdot(c_p\bar{\rho}\bar{\theta}\nabla\pi_b) = \partial B/\partial z. \tag{13b}$$

Using these results, we write Eq. (11) as

$$\frac{\partial w}{\partial t} = -\mathbf{v}\cdot\nabla w - c_p\bar{\theta}\frac{\partial \pi_{dn}}{\partial z} + \left[-c_p\bar{\theta}\frac{\partial \pi_b}{\partial z} + B\right], \tag{14}$$

where the second and third terms on the right-hand side are termed the dynamics and buoyancy forcing, respectively.

Contour plots of the terms in Eq. (14) at $t = 120$ min, $z = 4$ km are shown in Fig. 14. The plot of the tendency term (Fig. 14a) shows that the vertical velocity is increasing on the updraft's south flank and decreasing on the north as it must for southward propagation. The advection (Fig. 14b) tends to reduce w everywhere and is approximately colocated with the updraft. The buoyancy forcing (Fig. 14d) is positive, but it is also colocated with (or slightly lagging) the updraft and so is not responsible for propagation. Figure 14c shows clearly that the dynamics forcing is strongly positive on the updraft's south flank and negative on the north, and so it is responsible for the southward propagation.

We inquire further into the nature of the dynamics forcing; expanding the right-hand side of Eq. (13a) we obtain the form

$$\nabla\cdot(c_p\bar{\rho}\bar{\theta}\nabla\pi_{dn}) = -2\bar{\rho}\left[\frac{\partial v}{\partial x}\frac{\partial u}{\partial y} + \frac{\partial u}{\partial z}\frac{\partial w}{\partial x} + \frac{\partial v}{\partial z}\frac{\partial w}{\partial y}\right] - \bar{\rho}\left[\left(\frac{\partial u}{\partial x}\right)^2 + \left(\frac{\partial v}{\partial y}\right)^2 + \left(\frac{\partial w}{\partial z}\right)^2 - \frac{d^2\ln\bar{\rho}}{\partial z^2}w^2\right]. \tag{15}$$

There are many ways to express the right-hand side of Eq. (15), but none is uniquely advantageous for all flow situations (Adrian, 1981). We believe that the above decomposition most clearly isolates the effects of storm rotation (see Appendix B for further discussion). We continue in the direction of Klemp and Rotunno [1983; see their Eq. (12a–c)] by considering the contribution to the dynamics pressure from the terms that involve fluid shear [first three terms on the right-hand side of Eq. (15)] and those that involve fluid extension. Thus we let $\pi_{dn} = \pi_s + \pi_e$ and solve two separate Poisson equations for π_s and π_e, respectively, as described by Klemp and Rotunno (1983). The results of this calculation are shown in Figs. 14e, f and demonstrate that the upward forcing on the updraft's south flank is due to the terms involving fluid shear.

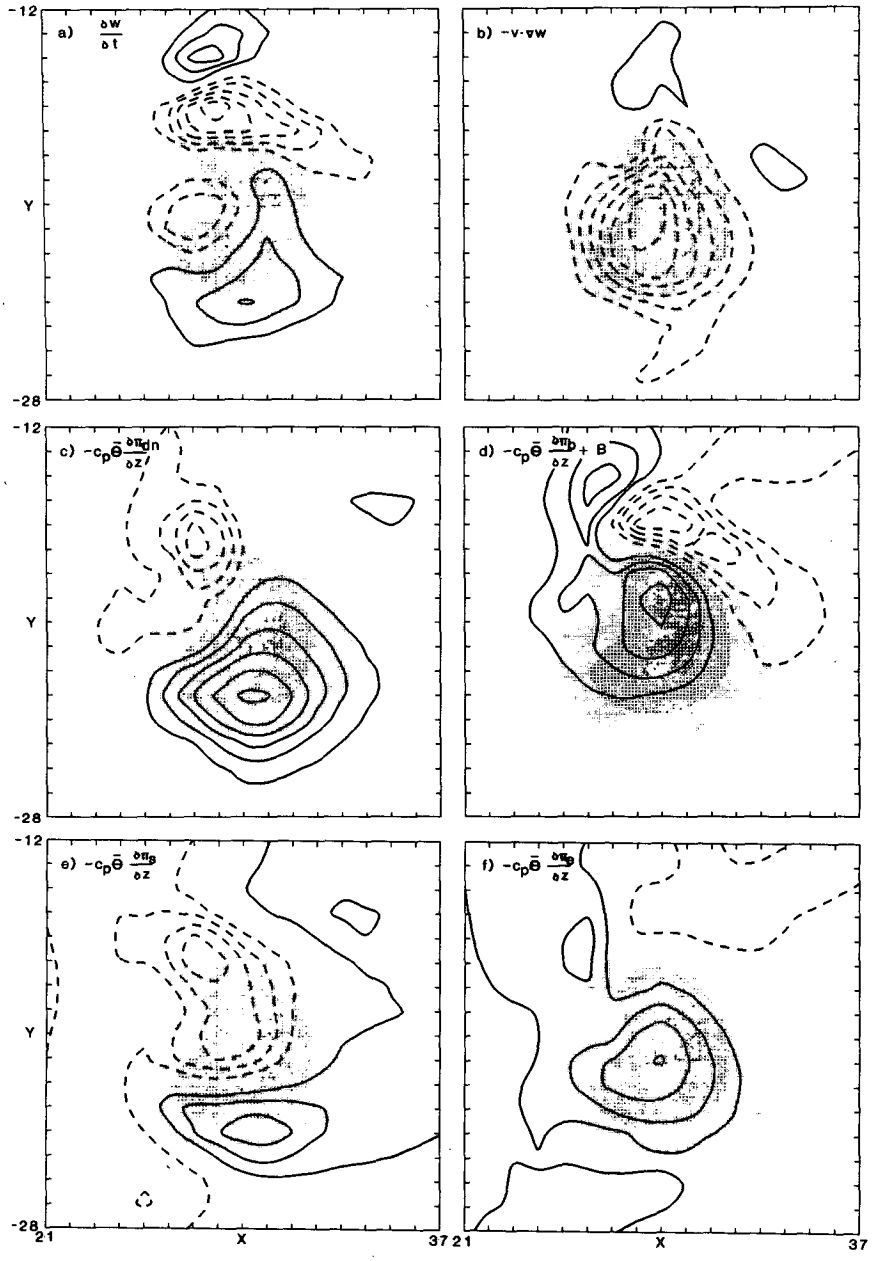

FIG. 14. Terms in vertical momentum equation: (a) tendency, (b) advection, (c) dynamics pressure acceleration, and (d) total buoyancy acceleration at t = 120 min and z = 4 km, and a decomposition of the dynamic pressure acceleration into the contribution from (e) shearing and (f) extension effects (contour interval = 0.01 m s^{-2} for all terms with zero line omitted). The vertical velocity is shaded in increments of 5 m s^{-1} beginning with the 5 m s^{-1} value.

The implication of the foregoing analysis is that the supercell propagates to the south mainly as a consequence of the midlevel updraft propagation with the low-level cold air spreading playing a secondary role. To test this notion we ran the numerical model with the rainmaking process set to zero; that is, condensation and the release of latent heat were allowed to occur, cloud droplets were allowed to form, but no precipitation was permitted. The progress of the updraft to the right of the mean wind in this simulation is shown in Fig. 15. Although the initial splitting process takes place more slowly and the low-level pattern is much different, the middle and upper level patterns are very similar between the cases with and without rain. Note that there is almost no rotation in the low-level flow. This is consistent with our thesis that a pool of cold air is required for the production of strong low-level rotation. This result

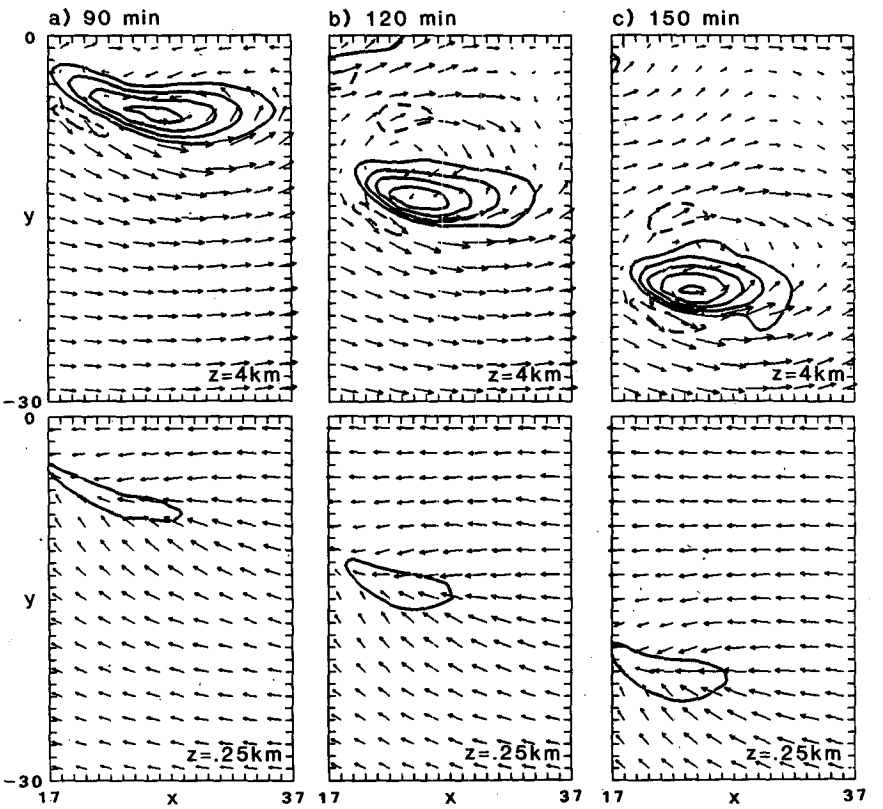

FIG. 15. As in Fig. 5 but for a simulation where no precipitation is permitted. The southward propagation still occurs without the cold outflow. Without the cold outflow, there is little indication of low-level rotation.

differs from that produced by WK in the simulation of a much weaker supercell storm. With much weaker dynamics forcing, splitting did not occur in the absence of rain processes.

A three-dimensional perspective (looking west) of the updraft and the perturbation pressure minimum from the no-rain simulation at $t = 150$ min is displayed in Fig. 16a. Thus, beneath the low pressure region on the south flank there is a favorable vertical pressure gradient helping low-level air to reach its LFC (level of free convection). The updraft, together with that part of the pressure minimum associated with the shearing effects described above, is shown in Fig. 16b. This shows that nearly all of the pressure drop at middle levels on the south flank is shear induced. Finally, the updraft together with the negative of the source term of the Poisson equation

$$2\bar{\rho}\left(\frac{\partial v}{\partial x}\frac{\partial u}{\partial y}+\frac{\partial u}{\partial z}\frac{\partial w}{\partial x}+\frac{\partial v}{\partial z}\frac{\partial w}{\partial y}\right),$$

which is solved to obtain the shear-induced pressure, is shown in Fig. 16c. It is positive and concentrated on the south flank.

With these results we can move beyond the purely formal mathematical analysis to obtain a physical understanding of what forces produce upward motion on the south flank of the updraft. We can obtain a crude picture of the pressure distribution for a given forcing function noting that $\nabla\cdot(c_p\bar{\rho}\bar{\theta}\nabla\pi) \approx -\pi$. Hence, from Eq. (15) we see that the extension terms produce positive pressure anomalies while the shearing terms produce either positive or negative anomalies. Since most of the fluid extension in an updraft occurs on its centerline, one would not expect significant vertical variations of this part of the pressure field on the flanks (where the dynamics forcing is strongest). Thus the explanation for the maximum upward forcing on the updraft flank exhibited by the dynamics forcing must lie with the shearing terms. Consider, for example, the term $\partial u/\partial z\cdot\partial w/\partial x$; if $\partial u/\partial z\cdot\partial w/\partial x > 0$, there is pure shearing motion, while if $\partial u/\partial z\cdot\partial w/\partial x < 0$, there is pure rotation (see Prandtl and Tietjens, 1934, their Figs. 52 and 53, p. 82). (For irrotational flow the shearing terms are all positive.) The negative pressure anomaly on the storm's right flank (Fig. 16a) is produced primarily by negative values of the shearing terms (Fig. 16c). Being negative, these terms are a measure of the local rotation in the flow. Thus, we conclude that the rightward storm propagation is driven by rotation (about both hori-

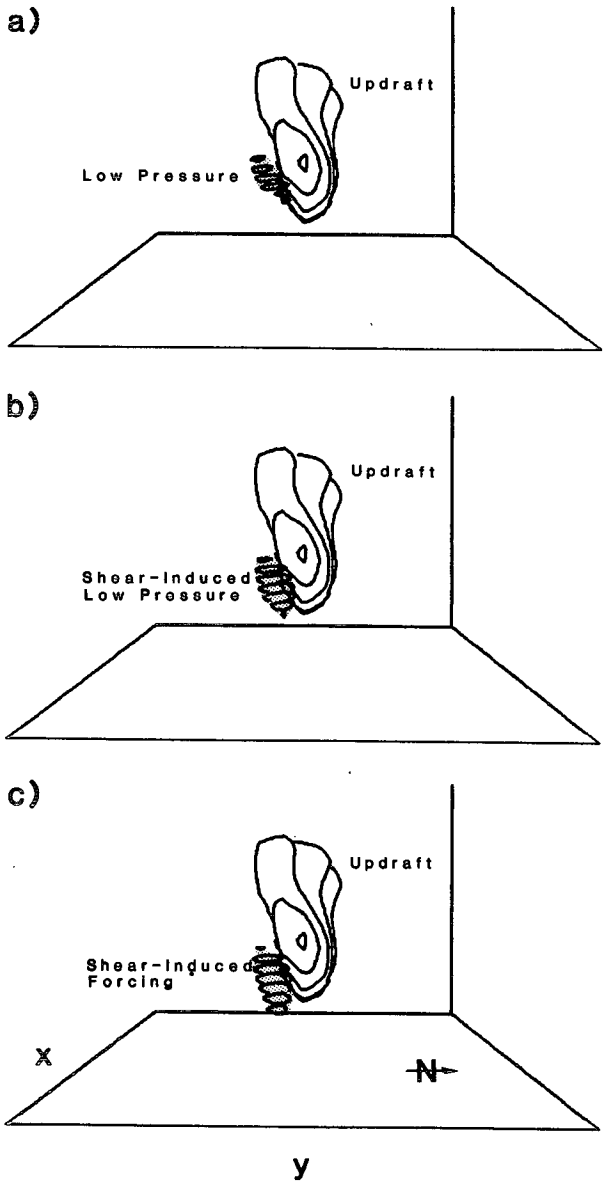

FIG. 16. A three-dimensional perspective (looking west) of the updraft (>20 m s^{-1}) together with (a) perturbation pressure (< −3.6 mb); (b) shear-induced pressure (< −3.6 mb); and (c) forcing associated with the shear terms (< −0.02, units irrelevant) for the no-precipitation simulation at t = 150 min on a 20 × 20 km portion of the computational domain. The vertical scale is exaggerated by a factor of 2.

zontal and vertical axes) generated on the storm's right flank.

In the present simulation, this rightward propagation is an inherently nonlinear effect. Rotunno and Klemp (1982) showed that the linear version of this term, $\partial u/\partial z \cdot \partial w/\partial x$, creates high pressure upshear and low pressure downshear of an updraft. Because the shear vector does not turn with height in the present case (i.e., $\partial V/\partial z = 0$), the linear effect will not produce any leftward or rightward propagation. However, the nonlinear part of the shear term does produce an elevated pressure low on the right flank which induces propagation in that direction. Consider that on the south flank of a rotating updraft, $\partial v/\partial x > 0$ and $\partial u/\partial y < 0$, so that $\partial v/\partial x \cdot \partial u/\partial y < 0$; $\partial v/\partial z < 0$ and $\partial w/\partial y > 0$, so that $\partial v/\partial z \cdot \partial w/\partial y < 0$; and $\partial w/\partial x \approx 0$, so that $\partial u/\partial z \cdot \partial w/\partial x \approx 0$. These terms should increase with height to some middle level, hence the elevated low pressure.

5. The wall cloud

Our theory that the low-level rotation is due to the presence of the cold air boundary (more precisely, a low-θ_e boundary) is also consistent with the formation of the wall cloud in the vicinity of the low-level rotation. In Fig. 17, the relevant low-level fields at t = 100 min—a time when the transition of the low-level updraft is in progress and vorticity is increasing rapidly (Fig. 2)—are displayed. The region of cloud-water greater than 0.1 g kg^{-1}, here identified as the model-equivalent wall cloud, is indicated in the figure along with the trajectory of the air that feeds the wall cloud at this time. Other familiar features already discussed in relation to Fig. 5 (Section 2) are evident.

Since supersaturation is not allowed in the cloud model microphysics, cloudwater is created wherever the mixing ratio of water vapor q_v equals the saturation mixing ratio q_{vs}. The wall, cloud together with a contour plot of q_v and shaded contours of w, is displayed in Fig. 18a. This figure shows that the air

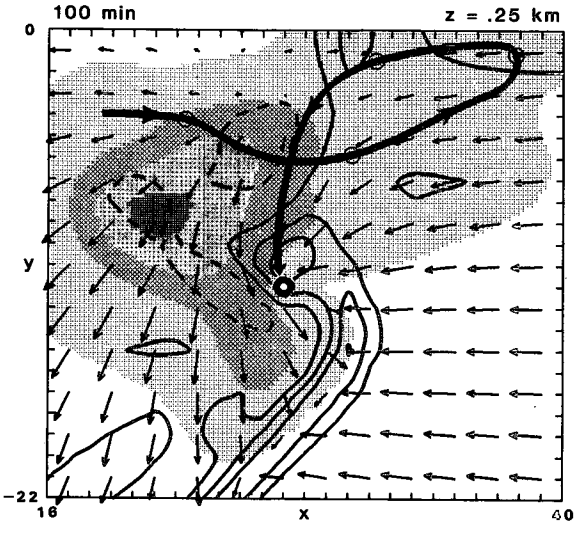

FIG. 17. The flow (represented as in Fig. 5b) at t = 100 min at z = 0.25 km with the region of cloudwater (>0.1 g kg^{-1}, thick solid contour) that we identify as the wall cloud. The thick solid line is a trajectory of the air which is at the location of the wall cloud at this time. The circles indicate the position of the air parcel, beginning at the upper left, at t = 20 (3.94 km), 40 (3.92 km), 60 (3.22 km) and 80 min (0.68 km).

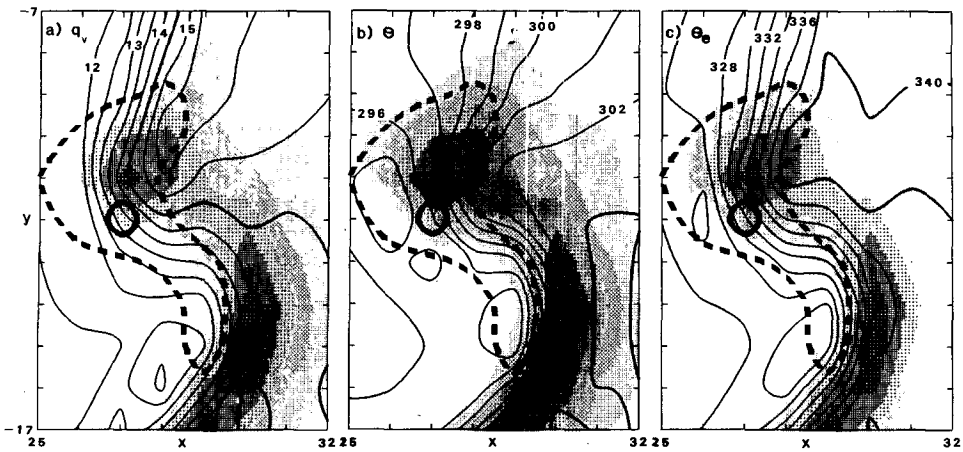

FIG. 18. Contours at z = 0.25 km of (a) mixing ratio, in intervals of 0.5 g kg^{-1}; (b) potential temperature, in intervals of 1 K; and (c) the equivalent potential temperature in intervals of 2 K, in a 7 × 10 km portion of the domain in the vicinity of the wall cloud. The updraft is represented by the shading in increments of 0.5 m s^{-1}. The thick circular line encloses the region where the cloudwater is greater than 0.1 g kg^{-1} (wall cloud). The thick dashed line encloses the region where the cloudwater is greater than 0.1 g kg^{-1} at z = 0.5 km.

composing the wall cloud has a mixing ratio of 13.2 g kg^{-1} and is thus drier than the ambient (14.5 gm kg^{-1}). Figure 18b displays the corresponding contours of potential temperature and shows that the air composing the wall cloud is much cooler than ambient. Figure 19 is an illustration of these saturation conditions, depicting q_{vs} versus θ computed from Teten's formula at the pressure p = 938 mb corresponding to the display level of z = 0.25 km. Thus saturation at this level (the wall cloud) occurs because the air, though absolutely drier, has 100% relative humidity due to the lower temperature. From Figs. 18a, b and 19, it is clear that the air to the west of the wall cloud is subsaturated despite its being cooler because it is too dry. Conversely, although the air to the east of the wall cloud is moister, it is subsaturated because it is too warm.

Obviously, the evaporation of rain produces the cool air near the surface. As rain evaporates into a volume of air, its mixing ratio increases as its temperature lowers. Because the air within the wall cloud is both cooler and dryer than the ambient air at z = 0.25 km, it must have originated at a higher level in the environment where the equivalent potential temperature is lower. The contour lines of θ_e reveal that the wall cloud has a much lower θ_e than does the ambient (Fig. 18c). Referring to Fig. 1, this air must have originated at some level above 3 km if θ_e were strictly conserved. Similar patterns of wet-bulb potential temperature were observed by Lemon (1974) and Barnes (1978) for severe thunderstorms using data from the National Severe Storms Laboratory (NSSL) surface mesonetwork.

The thick solid line in Fig. 17, representing the trajectory of the air parcel that composes the wall cloud, confirms that the air parcel originates at a height of approximately 4 km, consistent with the analysis of θ_e. Because the entire evolution of the storm occurs during the time the air parcel completes its journey from 4 km to the wall cloud, we display 20 min segments of the air parcel trajectory in Fig. 20 along with the velocity and rainwater fields at the

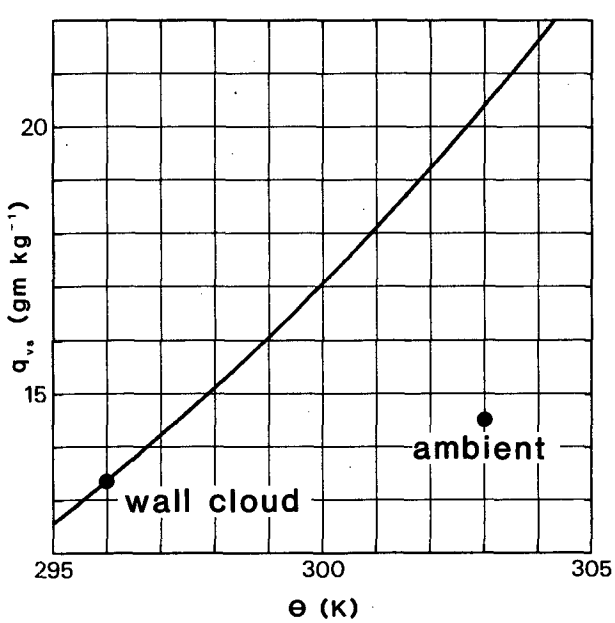

FIG. 19. The saturation mixing ratio q_{vs} vs θ computed from Teten's formula at a pressure corresponding to z = 0.25 km. The states of the wall cloud air and that of the undisturbed environment are indicated.

times and heights corresponding to the circles on the trajectory in Fig. 17.

At t = 20 min, the parcel is moving with the environmental flow from west to east at z = 3.94 km. The initial cell has not yet split and has its maximum vertical velocity on the center axis, and, as discussed in Section 3, there is cyclonic rotation associated with the updraft on the southern flank. The parcel continues to travel along the southern flank of the updraft at t = 40 min (z = 3.92 km) as the latter becomes elongated in the direction of shear. At this time, the air parcel begins to come under the influence of the cyclonic flow and turns toward the north. The accumulation of rainwater on the center axis, and dynamics pressure forcing on the flanks of the updraft, leads to the splitting of the initial updraft. By t = 60 min (z = 3.22 km), the parcel enters the rainy downdraft where evaporative cooling adds to the negative buoyancy of the rainloading and further promotes the downdraft. The parcel has descended to z = 0.68 km at t = 80 min. The updraft–downdraft system is now propagating to the south at a fairly steady rate while maintaining a mature supercellular structure. As the air parcel descends, it becomes moister and warmer, but upon reaching the ground it is still cooler and drier than the ambient low-level air. The subsequent ingestion of this air into the low-level updraft produces the wall cloud because of its lower lifted condensation level.

Incidentally, tail clouds (an often-observed appendage to the wall cloud) are observed to extend northward or northeastward into the cool air. Agee *et al.* (1977) concluded that this cloud is produced by the coolness of the air into which it extends. This is consistent with our theory for the wall cloud and further emphasizes the importance of the cool air boundary to the general problem.

6. Summary

Through analysis of the supercell-like convection produced by our three-dimensional cloud model in an idealized unidirectional-shear environment, we believe that we have reached a more fundamental understanding of supercell rotation and propagation. We have shown the way in which it follows from the conservation of equivalent potential vorticity that the elementary source of the middle-level rotation is the upward tilting of the environmental horizontal vorticity by the southward-propagating updraft. Low-level rotation derives from upward tilting of baroclinically-generated horizontal vorticity along the cool air boundary situated upstream of the low-level updraft. The relation between the low-level and midlevel fields of rotation is, therefore, not so obvious, for we saw in the special no-rain simulation (Fig. 15) that the midlevel updraft rotated just as well without the low-level rotation (produced by the cool air boundary which is absent in this case). Based on the foregoing results, it seems that the primary importance of the midlevel rotation is to transport potentially cold air to the forward and left flanks, where it, being evaporatively chilled by rain from the northward-sloping

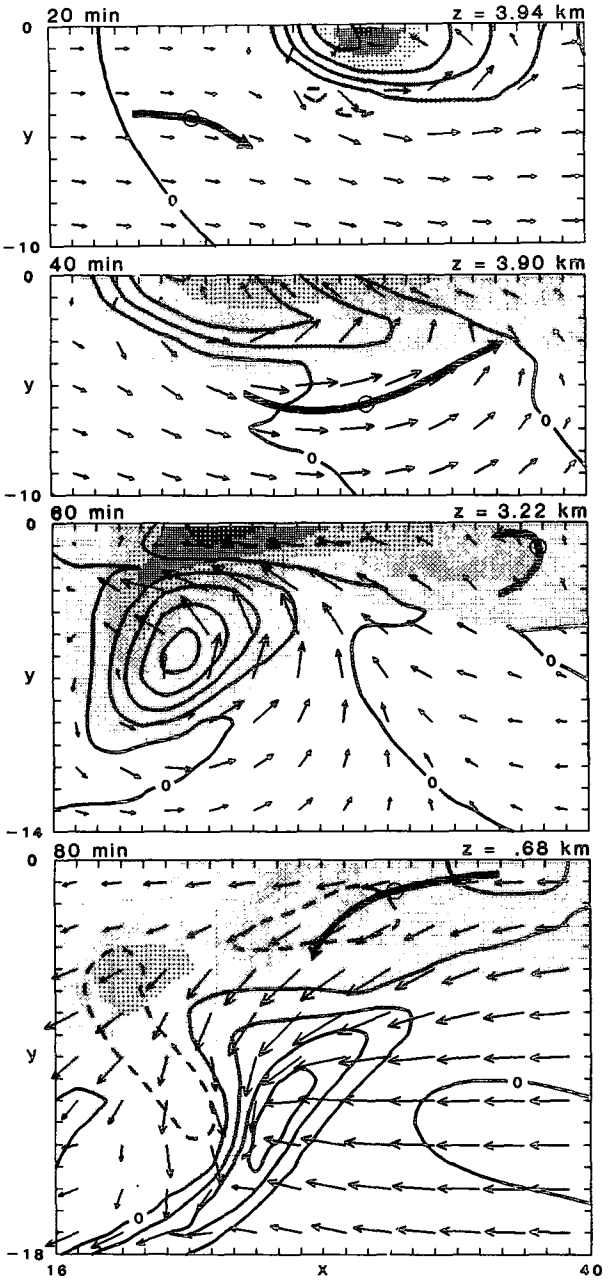

FIG. 20. The velocity and rainwater fields corresponding to the time and altitudes of the air parcel as indicated by the circles along the trajectory shown in Fig. 17. For t = 20, 40 and 60 min, the vertical velocity is contoured in intervals of 4 m s^{-1} and for t = 80 min the interval is 2 m s^{-1}. A horizontal velocity vector of one grid length corresponds to a magnitude of 7 m s^{-1} and the shading of the rain field is in increments of 2 g kg^{-1}. The thick solid line indicates 20-min portions of the air parcel trajectory.

updraft, descends and forms a cold pool on the left and forward flanks. This is just the right place for baroclinically-generated horizontal vorticity of the proper sign to produce positive vertical vorticity when this air subsequently encounters the low-level updraft.

The analysis of the circulation around a material curve surrounding the low-level maximum of vertical vorticity further emphasizes the importance of the presence of cold air for the development of low-level rotation. We believe this helps to conciliate theorists and observers of tornadoes. For many years observers have insisted that tornadoes do not reach maturity until rain and downdrafts have occurred in the storm, and then the tornado is located near the downdraft (e.g., Ward, 1961; Fujita, 1975; Lemon and Doswell, 1979). Theorists have focused, until recently, on the way in which axisymmetric updrafts produce intense vortices given an ambient circulation (see, e.g., the review by Lewellen, 1976). In view of Figs. 10 and 11, the resolution is easy: the cool rainy downdraft is necessary to produce the circulation on the material curve which eventually enters the low-level updraft. The formation of the pronounced lowered cloud base known as the wall cloud is consistent with this picture. The cool, dry outflow air drawn into the updraft at low levels is closer to saturation in spite of its being drier than the inflow air because it is cooler. The quasi-steady uplift of this negatively-buoyant air is a consequence of the strong dynamical forcing.

Of course, the tornado is typically an order of magnitude smaller than our horizontal grid size, and so the manner in which a flow like the one in Fig. 10 produces a tornado is a matter for further study. Klemp and Rotunno (1983) took a step in this direction by increasing the horizontal resolution in the simulation of the Del City storm (Klemp *et al.*, 1981) to 250 m and running the model over a smaller domain (13.5 km on a side) for a short period (10 min). The model produced many of the smaller-scale flow features of a mesocyclone that produces tornadoes; however, the resolution was still too coarse to capture any of the features of that nearly axisymmetric, rotating funnel of cloud or debris that we call the tornado. On this scale, the axisymmetric models are the only ones economically feasible at this time, but relating these results to even the intermediate Klemp–Rotunno model remains to be done.

The thunderstorm was found to propagate rightward by means of a favorable dynamic vertical pressure gradient induced to the right of the updraft by storm rotation. On the face of it, this sounds very much like the Magnus-effect type of argument (Fujita and Grandoso, 1968; Kuo, 1969); however, it is fundamentally different. The Magnus-effect is a force acting on a rotating cylinder in a direction perpendicular to the axis of the cylinder and to the direction of the flow past the cylinder. But clearly the updraft, in our case, does not "move" laterally because it is somehow pushed in that direction by a horizontal pressure gradient. It moves laterally because it continually grows on one side and decays on the other through the action of the vertical pressure gradient. What we do share with the earlier work is the idea that rightward propagation is primarily due to the interaction of the updraft at midlevels with the mean flow; the effects of the spreading cold air pool is secondary. If this is so, new analytical solutions, unencumbered by the inherent complications of rain processes, may yet be obtainable for this problem. Our work proceeds apace in this direction.

APPENDIX A

Equivalent Potential Vorticity

The derivation of Eq. (6) is straightforward (e.g., Dutton, 1976, p. 381), but a few caveats are in order: 1) θ_e is only approximately conserved, even in the absence of mixing (see the discussion on pp. 1073–1074 of Klemp and Wilhelmson, 1978a). 2) Granting the conservation of θ_e, and using the deep, anelastic continuity equation $\nabla\cdot(\bar{\rho}\mathbf{v}) = 0$, one can show that

$$\frac{d}{dt}\left\{\frac{\omega\cdot\nabla\theta_e}{\bar{\rho}}\right\} = \frac{\nabla\times(B\mathbf{k})\cdot\nabla\theta_e}{\bar{\rho}} = -\frac{1}{\bar{\rho}}J(B,\theta_e). \quad \text{(A1)}$$

If $J(B, \theta_e) = 0$, Eq. (6) is obtained. This will be true if $B = B(\theta_e)$ or if $\nabla_H B = 0$ or $\nabla_H\theta_e = 0$. Where the air is saturated, $B = B(\theta_e)$ and Eq. (6) is valid. In unsaturated portions of the storm, Eq. (6) remains approximately valid since $J(B, \theta_e)$ remains small. Over the lower portion of the storm, which contains the important rotational features, the patterns of B and θ_e are nearly congruent so that $J(B, \theta_e) = 0$. The reason for this is that at a given level, the cool air is low-θ_e air with a greater ability to evaporate rain before saturating. On the other hand, the warm air is high-θ_e air with a greater potential for latent heating. In places where the patterns of B and θ_e are not congruent, we determined that $J(B, \theta_e)$ is small. Estimating the order of magnitude of terms in Eq. (A1), we find that the constituent terms in $\omega\cdot\nabla\theta_e$ are typically

$$|\zeta|\left|\frac{\partial\theta_e}{\partial z}\right| \sim |\omega_H||\nabla_H\theta_e|$$

$$\sim (10^{-2}\ \mathrm{s^{-1}})(10^{-2}\ \mathrm{K\ m^{-1}}) \sim 10^{-4}\ \mathrm{K\ m^{-1}\ s^{-1}},$$

while the corresponding forcing term $J(B, \theta_e)$ has magnitudes

$$J(B,\theta_e) \sim 0(10^{-8}\ \mathrm{K\ m^{-1}\ s^{-2}}).$$

Because air parcels typically remain within these regions for a much shorter time than that required to change the equivalent potential vorticity by 10^{-5} K m^{-1} s^{-1} (1000 s), the influence of this effect is negligible. 3) There is a small (in the above sense)

amount of equivalent potential vorticity associated with the initial thermal disturbance.

In spite of these limitations, the predictions made assuming that $\omega \cdot \nabla \theta_e \approx 0$ are useful for obtaining a qualitative understanding of storm rotation. The fact that the vortex lines adhere so closely to θ_e surfaces in the model storm (cf. Figs. 7 and 9) further supports the approximate validity of Eq. (6).

APPENDIX B

Decomposition of the Pressure Equation

Equation (15) may be written in tensor notation [neglecting the variation of $\bar{\rho}(z)$ for simplicity] as

$$-\frac{\partial}{\partial x_i} c_p \bar{\theta} \frac{\partial \pi}{\partial x_i} = e_{ij} e_{ji} - \frac{1}{2} \omega_i \omega_i, \tag{B1}$$

where

$$e_{ij} = \frac{1}{2}\left(\frac{\partial u_i}{\partial x_j} + \frac{\partial u_j}{\partial x_i}\right) \tag{B2}$$

is the rate of strain tensor and ω_i is the vorticity vector. At first glance, Eq. (B1) may look preferable to Eq. (15) because (roughly speaking) according to Eq. (B1) fluid strain is associated with a positive pressure anomaly while fluid rotation is associated with a negative pressure anomaly.

Consider, for example, a two-dimensional flow. The terms on the right-hand side of Eq. (B1) may be written

$$e_{ij} e_{ji} = \left(\frac{\partial u}{\partial x}\right)^2 + \left(\frac{\partial v}{\partial y}\right)^2 + \frac{1}{2}\left(\frac{\partial v}{\partial x}\right)^2 + \frac{1}{2}\left(\frac{\partial u}{\partial y}\right)^2 + \frac{\partial u}{\partial y}\frac{\partial v}{\partial x}, \tag{B3}$$

$$-\frac{1}{2}\omega_i \omega_i = -\frac{1}{2}\left(\frac{\partial v}{\partial x}\right)^2 - \frac{1}{2}\left(\frac{\partial u}{\partial y}\right)^2 + \frac{\partial u}{\partial y}\frac{\partial v}{\partial x}. \tag{B4}$$

For a flow in solid-body rotation, $v = \alpha x$, $u = -\alpha y$, $e_{ij}e_{ji} = 0$ and $-\omega_i\omega_i = -2\alpha^2$ which works out fine. However, for the shear flow, $u = \alpha y$, $v = 0$, $e_{ij}e_{ji} = \alpha^2/2$ and $-\omega_i\omega_i = -\alpha^2/2$. Although these obviously sum to zero and produce the desired result, one is put in the awkward position of having to say that in the shear layer fluid strain is associated with positive pressure anomalies which are exactly cancelled by the negative pressure anomalies associated with fluid rotation.

Inspection of Eqs. (B3) and (B4) shows that two of the terms involving fluid shear identically cancel and only the term $\partial u/\partial y \partial v/\partial x$ ultimately contributes. These problems are avoided when Eq. (15) is used.

REFERENCES

Adrian, R. J., 1981: Comment on "A note on Poisson's equation for pressure in a turbulent flow." *Phys. Fluids,* **25,** 577.

Agee, E. M., J. T. Snow, F. S. Nickerson, P. R. Clare, C. R. Church and L. A. Schaal, 1977: An observational study of the West Lafayette, Indiana, Tornado of 20 March 1976. *Mon. Wea. Rev.,* **105,** 893–907.

Barnes, S. L., 1970: Some aspects of a severe, right-moving thunderstorm deduced from mesonetwork Rawinsonde observations. *J. Atmos. Sci.,* **27,** 634–678.

——, 1978: Oklahoma thunderstorms on 29–30 April 1970. Part I: Morphology of a tornadic storm. *Mon. Wea. Rev.,* **106,** 673–684.

Batchelor, G. K., 1967: *An Introduction to Fluid Dynamics.* Cambridge University Press, 615 pp.

Bluestein, H. B., and C. S. Sohl, 1979: Some observations of a splitting severe thunderstorm. *Mon. Wea. Rev.,* **107,** 861–873.

Browning, K. A., 1964: Airflow and precipitation trajectories within severe local storms which travel to the right of the mean wind. *J. Atmos. Sci.,* **21,** 634–639.

——, 1965: The evolution of tornadic storms. *J. Atmos. Sci.,* **22,** 664–668.

——, 1968: The organization of severe local storms. *Weather,* **23,** 429–434.

Burgess, D. W., 1974: Study of a severe right-moving thunderstorm utilizing new single Doppler radar evidence. M.A. thesis, Dept. of Meteor., University of Oklahoma Graduate College, 77 pp.

——, V. T. Wood and R. A. Brown, 1982: Mesocyclone evolution statistics. *Proc. 12th Conf. on Severe Local Storms,* San Antonio, Amer. Meteor. Soc., 422–424.

Clark, T. L., 1979: Numerical simulations with a three-dimensional cloud model: Lateral boundary condition experiments and multicellular severe storm simulations. *J. Atmos. Sci.,* **36,** 2191–2215.

Davies-Jones, R. P., 1983: The onset of rotation in thunderstorms. *Preprints 13th Conf. on Severe Local Storms,* Tulsa, Amer. Meteor. Soc., 215–218.

Dutton, J. A., 1976: *The Ceaseless Wind,* McGraw-Hill, 579 pp.

Eliassen, A., and E. Kleinschmidt, 1957: Dynamic meteorology, *Handbuch der Physik,* **58,** Springer-Verlag, 1–154.

Fankhauser, J. C., 1971: Thunderstorm–environment interactions determined from aircraft and radar observations. *Mon. Wea. Rev.,* **99,** 171–192.

——, G. M. Barnes, L. J. Miller and P. M. Roskowski, 1983: Photographic documentation of some distinctive cloud forms observed beneath a large cumulonimbus. *Bull. Amer. Meteor. Soc.,* **64,** 450–462.

Fujita, T., 1959: *Detailed analysis of the Fargo Tornadoes of June 20, 1957.* University of Chicago Tech. Rep. No. 5 to U.S. Weather Bureau, The University of Chicago, 29 pp.

——, 1975: Proposed mechanism of tornado formation from rotating thunderstorm. *Preprints, 9th Conf. on Severe Local Storms,* Norman, Amer. Meteor. Soc., 191–196.

——, and H. Grandoso, 1968: Split of a thunderstorm into anticyclonic and cyclonic storms and their motion as determined from numerical model experiments. *J. Atmos. Sci.,* **25,** 416–439.

Golden, J. H., and D. Purcell, 1978: Life cycle of the Union City, Oklahoma tornado and comparison with waterspouts. *Mon. Wea. Rev.,* **106,** 3–11.

Klemp, J. B., and R. B. Wilhelmson, 1978a: The simulation of three-dimensional convective storm dynamics. *J. Atmos. Sci.,* **35,** 1070–1096.

——, and ——, 1978b: Simulations of right- and left-moving storms produced through storm splitting. *J. Atmos. Sci.,* **35,** 1097–1110.

——, —— and P. S. Ray, 1981: Observed and numerically simulated structure of a mature supercell thunderstorm. *J. Atmos. Sci.,* **38,** 1558–1580.

——, and R. Rotunno, 1983: A study of the tornadic region within a supercell thunderstorm. *J. Atmos. Sci.,* **40,** 359–377.

Kuo, H.-L., 1969: Motions of vortices and circulating cylinder in shear flow with friction. *J. Atmos. Sci.,* **26,** 390–398.

Lemon, L. R., 1974: Interaction of two convective scales within a severe thunderstorm: A case study. NOAA Tech. Memo. ERL NSSL-71, U.S. Dept. of Commerce National Severe Storms Laboratory, Norman, OK, 1–16.

——, 1976: The flanking line, a severe thunderstorm intensification source. *J. Atmos. Sci.*, **33,** 686–694.

——, 1980: Severe thunderstorm radar identification techniques and warning criteria. NOAA Tech. Memo. NWS N SSFC-3, NSSL, Kansas City, KA, 60 pp. [Available from U.S. Dept. of Commerce, Sills Bldg., 5285 Port Royal Road, Springfield, VA, 22151.]

——, D. W. Burgess and R. A. Brown, 1975: Tornado production and storm sustenance. *Preprints, 9th Conf. on Severe Local Storms,* Norman, Amer. Meteor. Soc., 100–104.

——, and C. A. Doswell III, 1979: Severe thunderstorm evolution and mesocyclone structure as related to tornadogenesis. *Mon. Wea. Rev.*, **107,** 1184–1197.

Lewellen, W. S., 1976: Theoretical Models of the tornado vortex. *Proc. Symp. on Tornadoes: Assessment of Knowledge and Implications for Man,* Lubbock, Texas Tech University, 107–143.

Lilly, D. K., 1982: The development and maintenance of rotation in convective storms, *Intense Atmospheric Vortices,* L. Bergtsson and M. J. Lighthill, Eds, Springer-Verlag, Berlin, 149–160.

Maddox, R. A., 1976: An evaluation of tornado proximity wind and stability data. *Mon. Wea. Rev.*, **104,** 133–142.

Moller, Alan R., 1978: The improved NWS storm spotters' training program at Ft. Worth, Texas. *Bull. Amer. Meteor. Soc.*, **59,** 1574–1582.

Prandtl, L., and Tietjens, O. G., 1934: *Fundamentals of Hydro- and Aero-Mechanics,* Dover, NY, 270 pp.

Rotunno, R., 1981: On the evolution of thunderstorm rotation. *Mon. Wea. Rev.*, **109,** 577–586.

——, and J. B. Klemp, 1982: The influence of the shear-induced pressure gradient on thunderstorm motion. *Mon. Wea. Rev.*, **110,** 136–151.

Schlesinger, R. E., 1975: A three-dimensional numerical model of an isolated deep convective cloud: Preliminary results. *J. Atmos. Sci.*, **32,** 934–957.

——, 1978: A three-dimensional numerical model of an isolated thunderstorm. Part I: Comparative experiments for variable ambient windshear. *J. Atmos. Sci.*, **35,** 690–713.

——, 1980: A three-dimensional numerical model of an isolated thunderstorm. Part II: Dynamics of updraft splitting and mesovortex couplet evolution. *J. Atmos. Sci.*, **37,** 395–420.

Thorpe, A. J., and M. J. Miller, 1978: Numerical simulations showing the role of the downdraught in cumulonimbus motion and splitting. *Quart. J. Roy. Meteor. Soc.*, **104,** 873–893.

Truesdell, C., 1954: *The Kinematics of Vorticity,* Indiana University Press, 232 pp.

Ward, N. B., 1961: Radar and surface observations of tornadoes of May 4, 1961. *Proc. 9th Weather Radar Conf.*, Kansas City, MO, Amer. Meteor. Soc., 175–180.

Weisman, M. L., and J. B. Klemp, 1982: The dependence of numerically simulated convective storms on vertical wind shear and buoyancy. *Mon. Wea. Rev.*, **110,** 504–520.

Wilhelmson, R. B., and J. B. Klemp, 1978: A numerical study of storm splitting that leads to long-lived storms. *J. Atmos. Sci.*, **35,** 1974–1986.

——, and J. B. Klemp, 1981: A three-dimensional numerical simulation of splitting severe storms on 3 April 1964. *J. Atmos. Sci.*, **38,** 1581–1600.